



# 1 **Insights into the vulnerability of vegetation to tephra** 2 **fallouts from interpretable machine learning and big** 3 **Earth observation data**

4 Sébastien Biass<sup>1,2</sup>, Susanna F. Jenkins<sup>1,3</sup>, William H. Aeberhard<sup>4</sup>, Pierre Delmelle<sup>5</sup>, Thomas  
5 Wilson<sup>6</sup>

6 <sup>1</sup> *Earth Observatory of Singapore, Nanyang Technological University, Singapore*

7 <sup>2</sup> *Department of Earth Sciences, University of Geneva, Switzerland*

8 <sup>3</sup> *Asian School of the Environment, Nanyang Technological University, Singapore*

9 <sup>4</sup> *Swiss Data Science Center, ETH Zürich, Switzerland*

10 <sup>5</sup> *Environmental Sciences, Earth and Life Institute, UCLouvain, Belgium*

11 <sup>6</sup> *School of Earth and the Environment, University of Canterbury, New Zealand*

12 Corresponding author: Sébastien Biass ([sebastien.biass@unige.ch](mailto:sebastien.biass@unige.ch))

13 **Keywords** : Big EO data ; interpretable machine learning ; volcanic hazards; vulnerability  
14 model; vegetation impact; natural hazards; disaster risk reduction; Google Earth Engine;

## 15 **Abstract**

16 Although the generally high fertility of volcanic soils is often seen as an opportunity, short-  
17 term consequences of eruptions on natural and cultivated vegetation are likely to be negative.

18 The empirical knowledge obtained from post-event impact assessments provides crucial  
19 insights into the range of parameters controlling impact and recovery of vegetation, but their  
20 limited coverage in time and space offers a limited sample of all possible eruptive and  
21 environmental conditions. Consequently, vegetation vulnerability remains largely  
22 unconstrained, thus impeding quantitative risk analyses.

23 Here, we explore how cloud-based big Earth Observation data, remote sensing and interpretable  
24 machine learning (ML) can provide a large-scale alternative to identify the nature of, and infer  
25 relationships between, drivers controlling vegetation impact and recovery. We present a  
26 methodology developed using Google Earth Engine to systematically revisit the impact of past



27 eruptions and constrain critical hazard and vulnerability parameters. Its application to the  
28 impact associated with the tephra fallout from the 2011 eruption of Cordón Caulle volcano  
29 (Chile) reveals its ability to capture different impact states as a function of hazard and  
30 environmental parameters and highlights feedbacks and thresholds controlling impact and  
31 recovery of both natural and cultivated vegetation. We therefore conclude that big EO data and  
32 machine learning complement existing impact datasets open the way to a new type of dynamic  
33 and large-scale vulnerability models.

## 34 **1. Introduction**

35 In 2015, more than 8% of the world's population lived within 100 km of a volcano that had a  
36 significant eruption during the Holocene (Freire et al., 2019). Current trends indicate that this  
37 exposure will increase with, for instance, the population in the two regions most exposed to  
38 volcanic hazards (i.e. SE Asia and Central America) having doubled since 1975 (Freire et al.,  
39 2019). Supporting up to 10% of the world's population, the fertility of volcanic soils partly  
40 contributes to these increasing demographics (Rampengan et al., 2016, Loughlin et al., 2018).  
41 However, farming systems remain subject to short-term negative impacts from volcanic hazards  
42 (Choumert and Phinélias, 2018; Few et al., 2017; Phillips et al., 2019; Sivarajan et al., 2017).  
43 Recent, modest-sized eruptions over the past decade have illustrated the large numbers of  
44 people affected by volcanic activity, and the losses associated with impacts to agriculture, in  
45 particular the crop subsector. For example, the 2020 VEI 4 (Volcanic Explosivity Index,  
46 Newhall and Self, 1982) eruption of Taal (Philippines) affected ~260,000 people and caused an  
47 estimated 63 million USD impact on agriculture (ReliefWeb, 2020), whereas the 2018 eruption  
48 of Fuego (Guatemala), also a VEI 4, indirectly affected ~1.7 million people and caused ~58  
49 million USD impact on agriculture (The World Bank, 2018). By comparison, a recent study by  
50 Jenkins et al (2022) estimates that on the island of Java in Indonesia only, a VEI 4 eruption has



51 a 50% probability of directly affecting  $\geq 5$  million people and  $\sim 700$  km<sup>2</sup> of crops, which  
52 increases to  $\sim 29$  million people and 12,000 km<sup>2</sup> of crops for an eruption of VEI 5.

53 The Food and Agriculture Organisation (FAO, 2018) notes how the absence of a systematic  
54 and in-depth documentation of the impacts of natural hazards on agriculture prevents acquiring  
55 a global understanding of their long-term direct and indirect as well as tangible and intangible  
56 consequences. This is especially true for volcanic risk. Our current knowledge of the  
57 vulnerability of agriculture to volcanic hazards comes from a combination of opportunistic  
58 field-based post-event impact assessments (post-EIA; e.g., Blake et al., 2015; Le Pennec et al.,  
59 2012; Magill et al., 2013; Phillips et al., 2019; Stewart et al., 2016; Wilson et al., 2011; Wilson  
60 et al., 2013) and even rarer experimental studies (e.g., Hotes et al., 2004; Ligot et al., *in prep.*).  
61 However, the generalisation of these empirical lessons is limited by two main aspects. Firstly,  
62 eruptions are relatively infrequent but display a wide range of behaviours, each of which has  
63 specific hazard, hazard characteristics, and impact mechanisms. Secondly, they occur over a  
64 large variety of climates and affect various vegetation types and agricultural practices.  
65 Damage/disruption states (DDS) derived from these data (e.g., Craig et al., 2021; Jenkins et al.,  
66 2015; **Table 1**) have contributed to identifying critical components of vulnerability, but  
67 currently remain too limited in time and space to allow for the development of accurate and  
68 generalised risk models.

69 Satellite-based Earth Observation (EO) data, on the other hand, provide a data acquisition  
70 framework that is both global in space and consistent in time. Missions such as Landsat,  
71 MODIS or Sentinel now provide five decades of global EO data at a constantly increasing  
72 spatial, temporal and spectral resolution. Monitoring of the spectral characteristics of vegetation  
73 using these missions has been used to assess the recovery of vegetation after earthquakes (Chou  
74 et al., 2009; Lu et al., 2012) and droughts (Rembold et al., 2019) or to derive global-scale



75 datasets to estimate food security (Meroni et al., 2019). In volcanic contexts, satellite imagery  
76 has been used to capture the impact of eruptions on vegetation (de Rose et al., 2011; Marzen et  
77 al., 2011; De Schutter et al., 2015; Easdale and Bruzzone, 2018; Li et al., 2018; Tortini et al.,  
78 2017). Although innovative, these attempts mostly relied on single case studies, simplified  
79 representations of hazards and never systematically investigated the range of factors controlling  
80 the impact and recovery. The dominant limitation behind this latter point is a data processing  
81 issue: despite the availability of an unprecedented variety of data through EO, this big EO large  
82 dataset is associated with new challenges regarding data access, storage and processing. These  
83 challenges have prevented the systematic investigation of the nature and the relationship  
84 between the various processes controlling vulnerability and impact of vegetation to volcanic  
85 hazard from a global remote sensing perspective.

86 However, the recent advent of cloud-based EO data storage and processing platforms paves the  
87 way for the development of methodologies that can exploit the full potential of big EO data  
88 (Giuliani et al., 2019; Gomes et al., 2020; Mahecha et al., 2020). Beyond providing a framework  
89 for data-intensive research, big EO data platforms contribute to systematically extracting and  
90 processing raw data into information and knowledge (Lehmann et al., 2020; Nativi et al., 2020;  
91 Rowley, 2007). Over the past five years, *Google Earth Engine* (GEE; Gorelick et al., 2017) has  
92 seen the highest increase in applications reported in the scientific literature. GEE provides  
93 access and a computing power to process big EO data enabling reproducible, global scale  
94 analyses (Tamiminia et al., 2020; Wang et al., 2020). GEE has been applied to aspects of natural  
95 vegetation dynamics (Campos-Taberner et al., 2018; Kong et al., 2019; Zhang et al., 2019),  
96 crop mapping and monitoring (Jin et al., 2019; Liu et al., 2020), land cover-land use  
97 classification (Khanal et al., 2020), food security (Poortinga et al., 2018; Rembold et al., 2019)  
98 and hazard mapping (Crowley et al., 2019; DeVries et al., 2020). In a volcanic context, the use  
99 of GEE remains limited to a few applications (e.g., Biass et al., 2021; Murphy et al., 2017).



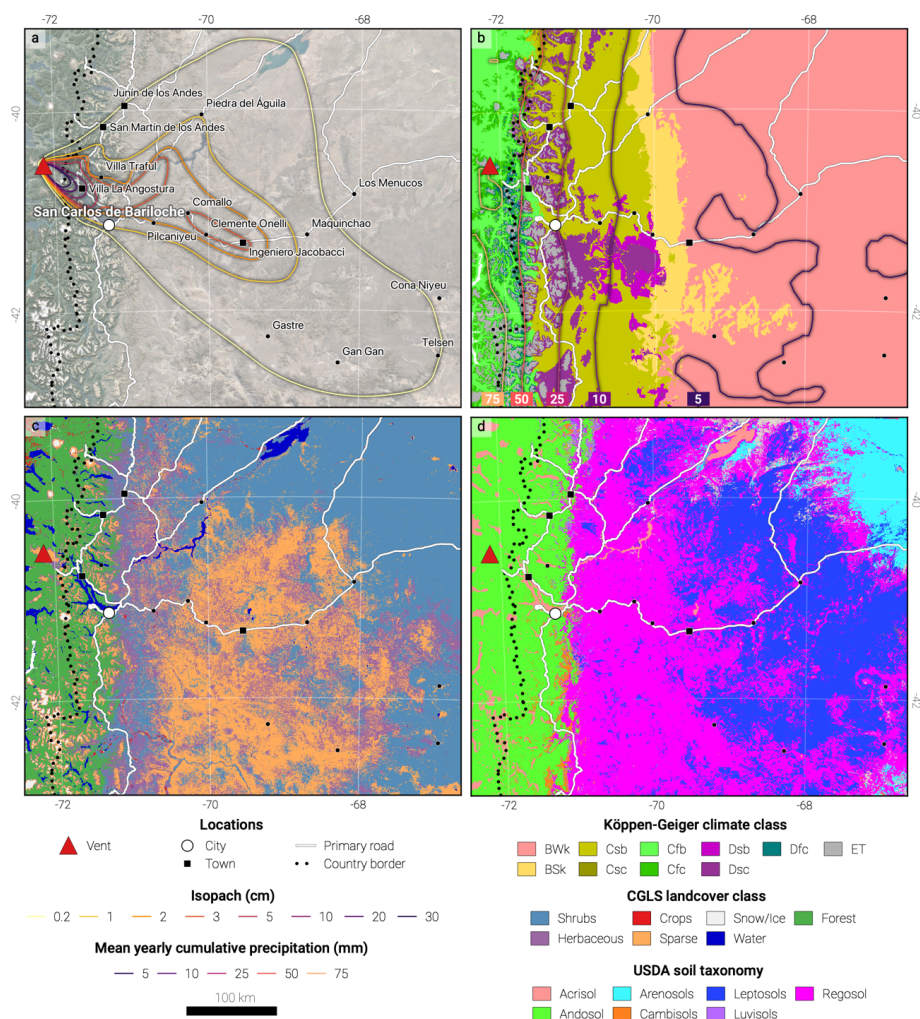
100 We argue that the advent of open-access cloud-based EO data platforms combined with  
101 increasingly efficient empirical modelling approaches offer an unprecedented opportunity to  
102 investigate the fragility of vegetation, including agricultural crops, to diverse events like  
103 volcanic eruptions, where field studies spanning the large spatial and temporal impact spaces  
104 are typically not possible. Here we lay the foundation of a methodology to extract previously  
105 unexploited knowledge about the impact to, and recovery of, vegetation from past eruptions  
106 recorded in archives of multi-spectral images. In line with the challenges identified by the FAO  
107 (FAO, 2018), this methodology is designed to support a framework to i) unify indirect, global  
108 with direct, *in situ* observations of impacts and ii) develop an innovative type of evidence-  
109 based, EO-driven vulnerability model. Both factors will improve our empirical knowledge  
110 around vegetation impacts and recovery following volcanic eruptions, supporting evidence-  
111 based assessments for future eruptions.

112 Here we focus on the impacts to vegetation caused by the widespread tephra fallout deposits  
113 from the 2011 eruption of Cordon Caulle volcano (Chile). The main steps include i)  
114 reconstructing the relevant hazard impact metrics of the associated tephra fallout deposit using  
115 dedicated numerical models, ii) mapping vegetation impact using time series of MODIS images  
116 retrieved from GEE, iii) identifying and processing selected datasets and variables on GEE to  
117 build up a big EO dataset of proxies capturing the dynamics of vulnerability in space and time,  
118 iv) developing a flexible machine learning (ML) algorithm to trained to explain impact as a  
119 function of the covariates and v) interpreting the model's result to investigate the nature,  
120 importance and relationships between the different hazard and vulnerability proxies using  
121 dedicated libraries.

122 **Table 1** : Damage/disruption states (DS1–5) as a function of the dry deposit thickness as hazard proxy identified  
123 by Jenkins et al., (2014) based on literature review. DDS assume that crops are in the growing stage. Hazard  
124 metrics include the median and interdecile deposit thicknesses inferred from expert judgement and empirical data.



125



126

127 Figure 1: Overview map of the study area. a Isopach (cm) from Dominguez and Baumann (personal  
 128 communication) showing lines of equal thickness of the fallout deposit for the month of June 2011. Locations are  
 129 those mentioned in Elissondo et al., (2016) as being affected by tephra fall. Background is © Google Maps 2022.  
 130 Roads, locations and borders are from © OpenStreetMap contributors 2021. Distributed under the Open Data  
 131 Commons Open Database License (ODbL) v1.0. b Mean yearly cumulative precipitations (mm) for the period  
 132 2006-2011 inferred from ERA5. Note that these values differ from those presented in the text and in Elissondo et  
 133 al., (2016) as ERA5 values represent averages over a model grid cell and time step. Background is the Köppen-  
 134 Geiger climate classification of Beck et al., (2018). *BWk* - Arid, desert, cold arid, *BSk* - Arid, steppe, cold arid, *Cfb*  
 135 - Warm temperate, fully humid, warm summer, *Cfc* - Warm temperate, fully humid, cool summer, *Csb* - Warm



136 temperate, summer dry, warm summer, *Csc* - Warm temperate, summer dry, cool summer, *Dsb* - Snow, summer  
137 dry, warm summer, *Dsc* - Snow, summer dry, cool summer, *ET* - Polar, polar tundra. **c** Landcover classes from  
138 the CGLS–LC1000 dataset (Buchhorn et al., 2020). **d** Dominant soil types in the study area from the SoilGrid  
139 dataset (Hengl et al., 2017) based on the USDA soil taxonomy. All maps are projected using EPSG:32719.

## 140 **2. Background**

### 141 **2.1. Impact of volcanic hazards on vegetation**

142 Explosive volcanic eruptions produce *tephra*, a generic term for pyroclasts originating from the  
143 fragmentation of parent magma, the fraction <2 mm diameter of which is referred to as *ash*. For  
144 sufficiently large eruptions, tephra deposits can alter the hydrology, vegetation cover and soil  
145 properties of entire region, contributing to the perturbation of their ecosystems for months-years  
146 (Major et al., 2016; Pierson et al., 2013). Direct negative impacts on, and the ability of  
147 vegetation to recover from eruptions depends on complex interactions between biotic and  
148 abiotic parameters (Ayrís and Delmelle, 2012; Arnalds, 2013). Biotic parameters include the  
149 type and composition of the vegetation, the biological legacy related to previous stresses and  
150 the phenological state of the plant at the time of eruption. Abiotic parameters include climate  
151 (e.g. rainfall and temperature) and environmental setting (e.g. elevation, slope, orientation)  
152 (Crisafulli et al., 2015; Dale et al., 2005). For crops, impacts also depend on access to  
153 technology and mitigation measures (Magill et al., 2013; Wilson et al., 2013a). Mechanisms of  
154 adverse effects of tephra on vegetation are various, including smothering and burial, breaking  
155 and abrasion, reduced photosynthesis, salt-induced stress and limitation of pollination (Arnalds,  
156 2013; Ayrís and Delmelle, 2012; Blake et al., 2015). Finally, impacts also depend on the  
157 characteristics of the eruption (e.g., magnitude, intensity and style) and the deposit (i.e.,  
158 thickness, grainsize distribution, content in water-soluble elements) (Cronin et al., 2014;  
159 Stewart et al., 2016). Overall, tephra on crops perturbate plant phenology and may decrease or  
160 even annihilate crop production (Ligot et al., submitted; Wilson et al., 2007).



## 161 **2.2. Case study: The Puyehue–Cordón Caulle 2011 eruption**

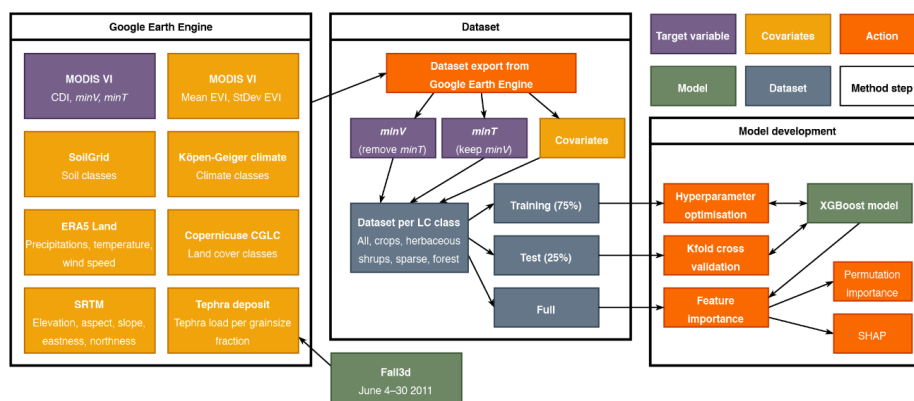
162 On June 4 2011, a subplinian rhyolitic eruption started at Cordón Caulle volcano (CC; 40.525  
163 S, 72.16 W; Figure 1), part of the Puyehue–Cordón Caulle volcanic complex. The eruption  
164 began with a 24–30 h–long paroxysmal phase that gradually transitioned to low intensity tephra  
165 emissions lasting for several months (Pistolesi et al., 2015). Reported plume heights ranged  
166 from 9–12 km asl for the first 3–4 days, 4–9 km asl for the following week and <4 km asl after  
167 June 14 (Bonadonna et al., 2015; Collini et al., 2013). During the first week, westerly winds  
168 dispersed ~1 km<sup>3</sup> of tephra towards Argentina. Published isopach maps describe the deposit  
169 thickness associated with various phases of the eruption (e.g. Bonadonna et al., 2015; Collini  
170 et al., 2013). An unpublished report by Dominguez and Baumann (personal communication),  
171 combining data from Bonadonna et al., (2015) and Pistolesi et al., (2015), shows the spatial  
172 distribution of total deposit thickness for June 4–30 2011 (Figure 1a). Levels of all water-  
173 extractable elements of the 2011 Cordón Caulle tephra were low to very-low (Stewart et al.,  
174 2016).

175 The deposit of the CC 2011 eruption impacted three different ecosystems: from west to east,  
176 southern Andes, Andean foothills and lowlands (Elissondo et al., 2016). These roughly  
177 correspond to the *Warm temperate – fully humid*, *Warm temperate – summer dry* and *Arid*  
178 climate classifications (Figure 1; Beck et al., 2018), respectively, each characterized by specific  
179 assemblages of vegetation (Easdale and Bruzzone, 2018; Enriquez et al., 2021). Southern Andes  
180 are characterized by a high elevation (mean of 2000 m asl), Valdivian temperate forest and  
181 annual precipitations of 800–2500 mm, mainly occurring in June–August (Elissondo et al.,  
182 2016). Andean foothills are characterized by a gradient of annual precipitation decreasing from  
183 800 in the west to 300 mm in the east and a vegetation of grasses, shrubs, and wet meadows  
184 covering 5–10 % of the area (Easdale and Bruzzone, 2018; Elissondo et al., 2016). The lowland  
185 is characterized by a cold and semi-arid climate with annual precipitations of ≤300 mm. During





186 the six years prior to the eruption, this region experienced <160 mm of precipitation per year,  
 187 which caused regional drought conditions. Due to water availability, the rainfall gradient  
 188 strongly controls the type of farming, with pastoral farming and agriculture in Andean regions  
 189 and low intensity goat and sheep farming in the arid lowlands (Stewart et al., 2016). In addition,  
 190 regions with low precipitations experience wind erosion and remobilization of loose tephra  
 191 (Dominguez et al., 2020b; Forte et al., 2017; Wilson et al., 2011).



192

193 **Figure 2** : Graphical summary of the model development. Flowchart made with diagrams.net.

### 194 3. Material and methods

195 **Figure 2** summarises the conceptual steps of our new methodology to investigate the effects of  
 196 tephra on vegetation using big EO data. The aim is to train a ML model to capture vegetation  
 197 impact inferred from multi-spectral satellite images and explain it as a function of covariates  
 198 describing hazard and vulnerability. We detail the successive steps of this methodology, from  
 199 the quantification of vegetation impact (Section 3.1) and covariates (Section 3.2) to the  
 200 development, application and interpretation of the ML model (Sections 3.3–**Error! Reference s**  
 201 **ource not found.**). Throughout the paper, we refer to metrics of vegetation impact as the *target*  
 202 *variable*, whereas *feature* is used as a synonym for *co-variate* and/or *explanatory variable*, and  
 203 *instance* as a synonym for a geographic *point*.



### 204 **3.1. Quantifying vegetation impact from remote sensing data**

205 *In situ* assessment of vegetation (including crops) impact is typically quantified using various  
206 metrics, depending on the purpose (e.g., percentage of destroyed vegetation or yield loss; **Table**  
207 **1**). We use the *Enhanced Vegetation Index* (EVI; Huete et al., 2002) as a remote sensing-based  
208 proxy for biomass production (Kong et al., 2019; Poortinga et al., 2018), and consider *impact*  
209 as a negative deviation of the post-eruption EVI signal. The EVI is retrieved from MODIS  
210 imagery (i.e., the MYD13Q1 and MOD13Q1 V6 products) generated every 16 days at a spatial  
211 resolution of 250 m. This MODIS image collection was processed on GEE.

#### 212 *3.1.1. Temporal smoothing*

213 The MODIS EVI image collection is temporally smoothed using the median pixel value over  
214 consecutive time steps. This approach to temporal smoothing, used to reduce artefacts, was  
215 selected over filtering-based (e.g., Savitski-Golay filters) or non-parametric statistical (e.g.  
216 double logistic function) methods for two main reasons. Firstly, these methods are sensitive to  
217 the density and the signal-to-noise ratio of the time series (Cai et al., 2017). As volcanoes are  
218 vast topographic edifices, frequent clouds in their vicinity makes the application of such  
219 algorithms unstable and unreliable. Secondly, we focus on the impacts occurring at a medium-  
220 term rather than in the immediate aftermath of an eruption, where a Vegetation Index (VI) can  
221 capture signals that do not record impact (e.g., increase in soil brightness due to tephra deposit).  
222 As a result, the median value over a given time window presents the most stable and  
223 conservative smoothing method around volcanoes. We test here two-time windows of 1 and 3  
224 months using the eruption date as a reference point.

#### 225 *3.1.2. Anomaly quantification*

226 Multiple approaches have been developed to quantify VI *anomalies* with various purposes  
227 ranging from early warning (e.g. Asoka and Mishra, 2015; Meroni et al., 2019; Rembold et al.,  
228 2019) to index-based parametric insurance (e.g. Martín-Sotoca et al., 2019). VI anomalies have



229 also been used to monitor vegetation recovery after natural hazards (e.g. fires, Bright et al.,  
230 2019; volcanic ashfall, De Schutter et al., 2015), cropping intensities (e.g. Liu et al., 2020) or  
231 long term land degradation (Gonzalez-Roglich et al., 2019) or changes in vegetation dynamics  
232 (Kalisa et al., 2019). We adapt the approach of Poortinga et al. (2018) as a proxy for impact of  
233 volcanic ash on vegetation, hereafter named Cumulative Difference Index (CDI). The CDI is  
234 computed as:

$$235 \quad CDI_{ijk} = \sum_{t=1}^t VI_{ijk} - \overline{VI_{ij}},$$

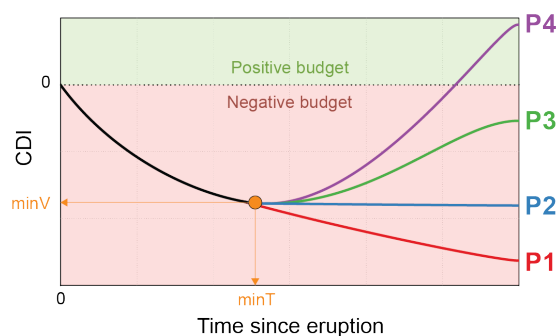
236 Equation 1

237 where  $CDI_{ijk}$  is the CDI value for pixel  $i$  during the time period  $j$  for year  $k$ ,  $VI_{ijk}$  is the VI  
238 value for pixel  $i$  during the time period  $j$  for year  $k$  and  $\overline{VI_{ij}}$  is the long-term VI mean over the  
239 baseline (averaged over 5 years prior to eruption for pixel  $i$  and period  $j$ ).  $VI$  is the vegetation  
240 index (here, EVI) and  $j$  is an arbitrary time window, referring to a subset of a year. Here,  $j$   
241 considers a 1–3-month period and the baseline considers 5 years of pre-eruption conditions.

242 The temporal evolution of the CDI is used as the metric for impact and recovery. **Figure 3**  
243 illustrates idealized profiles that the CDI can adopt through time. Following Equation 1, a  
244 scenario where  $CDI_{ijk}$  remains negative implies that post-eruption conditions are persistently  
245 lower than the baseline (i.e., negative CDI slope, P1 in **Figure 3**). A CDI flattening and reaching  
246 a zero gradient indicates a return to pre-eruption conditions (P2 in **Figure 3**). If the gradient of  
247 the CDI slope becomes positive after the inflection point, the post-eruption biomass production  
248 has exceeded pre-eruption conditions. If the CDI curve flattens at a negative CDI value, the  
249 total loss in biomass due to the eruption has been partly compensated by a temporary increase  
250 (P3 in **Figure 3**). Should the absolute CDI value become positive, the total biomass loss caused  
251 by the eruption has been either compensated or exceeded by the gains (P4 in **Figure 3**). The



252 purpose of the model is to explore conditions explaining the magnitude of impact (i.e.,  $minV$  in  
253 **Figure 3**) and the duration to reach it (i.e.,  $minT$  in **Figure 3**). The shape of the CDI curve after  
254 reaching  $minV$  is not considered here, and  $minV$  for the case of P1 in **Figure 3** is the minimum  
255 value reached after 5 years post-eruption.



256

257 **Figure 3:** Illustration of various possible CDI profiles through time.  $minV$  represents the minimum CDI value  
258 reached by a CDI profile and  $minT$  the duration after which  $minV$  has been reached. P1 represents a scenario with  
259 a permanent degradation of the EVI. P2 represents a scenario where post-eruption conditions have returned and  
260 remain equal to pre-eruption conditions. P3 represents a scenario where post-eruption conditions have returned  
261 and temporarily exceeded pre-eruption conditions without compensating for the deficit caused by the eruption. P4  
262 is similar to P3, but with post-eruption conditions sufficiently persisting to compensate and exceed the deficit  
263 caused by the eruption.

264 **Table 2 :** Summary of variables used in the model.

### 265 3.2. Model features

266 Co-variates used in the model to predict the impact (**Table 2**) were chosen to capture the  
267 relevant hazard and vulnerability parameters identified from literature (Section 2.1). Most  
268 datasets are natively available on GEE, and others have been manually uploaded as assets. Note  
269 that the original covariate dataset contained ~300 features. Here are presented the final set of  
270 variables identified based on i) a minimum degree of relations in an exploratory data analysis  
271 phase and ii) an iteration of the process of model optimisation and computation of feature



272 importance described in section 3.4.3 that allowed identifying and retaining the most  
273 informative variables.

274 **Table 3** : Initial parameters to the Fall3d runs. For the Suzuki plume model,  $A$  and  $\lambda$  are the shape factor controlling  
275 the mass distribution described by Pfeiffer et al. (2005), where  $\lambda=2$  results in more mass distributed in the lower  
276 portion of the plume. The *FPlume* approach (Folch et al., 2016) was solved for mass flow rate (MFR, Degruyter  
277 and Bonadonna (2012). Two total grain-size distributions (TGSD) were tested including a field-based Gaussian  
278 ( $Md \Phi$  and  $\sigma \Phi$  of 1.7 and 3.1, respectively; Bonadonna et al., 2015) and a model-based Bi-Weibull (modes at -  
279 3.13 and 4.69  $\Phi$  with respective shape factors of 0.73 and 1.1  $\Phi$  and a mixing factor of 0.64; Costa et al., 2016,  
280 Folch et al., 2021) distributions.

### 281 3.2.1. Deposit properties

282 Deposit thickness and grain-size distribution are the two of the main physical aspects  
283 controlling the direct impact of ashfall on vegetation (e.g., Jenkins et al., 2015). Since available  
284 isopach maps represent only deposit thickness, we reconstructed the grainsize distribution of  
285 the deposit associated with the June 4-30 2011 phase of the CC2011 eruption using Fall3D  
286 v8.0.1 (Folch et al., 2021). The model was initialised using hourly atmospheric conditions  
287 retrieved from the European Centre for Medium-Range Weather Forecasts (ECMWF) ERA5  
288 dataset (Hersbach et al., 2020) and daily mean plume heights reported by Collini et al. (2013).  
289 We tested several modelling schemes (**Table 3**) and compared the outputs against the isopach  
290 in Figure 1a. For this, isopachs were interpolated using a generalised additive model and  
291 converted to maps of tephra accumulation using a constant deposit density. We tested densities  
292 of 1000, 2000 and 2200 kg/m<sup>2</sup> to provide a range of tephra thicknesses for each point. The  
293 Fall3D *NetCDF* output was converted to a multiband *geotif* with each band containing mass  
294 loads for different size fractions. Size fractions computed by Fall3D were grouped into *lapilli*  
295 (2–64 mm), *coarse ash* (1-0.25 mm) and *fine ash* (<0.25 mm). The *geotif* was uploaded as an  
296 asset to GEE.



297 3.2.2. *Climate*

298 Atmospheric data were obtained from GEE using the ERA5 Land monthly averaged climate  
299 dataset (Hersbach et al., 2020), which provides a global reanalysis of climate variables since  
300 1981 at a spatial resolution of  $0.1 \times 0.1^\circ$ . The total precipitation and the surface air temperature  
301 were retrieved and their mean computed over 1, 2, 3, 6 and 12 months before the eruption. Each  
302 variable is included both as raw values and anomalies computed as the Stand Regeneration  
303 Index (SRI; Hope et al., 2012). As for CDI, we used a 5-years pre-eruption baseline and  
304 normalized the closest pre-eruption value  $V_{ijk}$  by the mean value over the same period in the  
305 baseline  $V_{ij}$ :

306 
$$SRI_{ijk} = \frac{V_{ijk}}{V_{ij}}$$

307 Equation 2

308 The model also includes the wind velocity at the time of the eruption from the ERA5 Land  
309 dataset.

310 In addition to atmospheric variables, the model includes Beck et al., (2018)'s updated 1-km  
311 version of the Köppen-Geiger climate classification. The study area spans three of the five main  
312 categories (*Arid*, *Warm temperate* and *Polar*), with two sub-types of the *Arid* (i.e. *Desert – hot*  
313 *arid* and *Steppe – hot arid*) and four sub-types of the *Warm temperate* (*fully humid – warm*  
314 *summer*, *fully humid – cold summer*, *summer dry – warm summer*, *summer dry – cool summer*).  
315 A *One Hot Encoding* procedure was applied to this dataset to transform categorical labels into  
316 the numerical values required by most ML algorithms.

317 3.2.3. *Terrain*

318 Terrain data were obtained from the Shuttle Radar Topography Mission (SRTM; Farr et al.,  
319 2007) using the NASA's SRTM V3 product at a resolution of  $\sim 30$  m. Elevation, slope, aspect,



320 eastness and northness (*sine* and *cosine* of aspect, respectively) were retrieved from GEE and  
321 used as features.

#### 322 3.2.4. Landcover

323 Landcover was obtained from Copernicus Global Land Service (CGLS) Dynamic Land Cover  
324 map (CGLS-LC1000, Buchhorn et al., 2020), available on GEE at a spatial resolution of 100 m  
325 yearly from 2015-2019. The landcover type is retrieved from the *discrete\_classification* band  
326 for the closest year to the eruption (here 2015). To test the impact of tephra on various types of  
327 vegetation, we extracted the *Cultivated and managed vegetation/agriculture* class as a proxy  
328 for cropland and the *Shrubs*, *Sparse* and *Herbaceous vegetation* classes (i.e., values 40, 20, 60  
329 and 30, respectively). In addition, we extracted a composite *Forest* class comprising all classes  
330 tagged with *Forest*. In the study area, present forest classes include *Evergreen broad leaf*, both  
331 *Closed* (112) and *Open* (122), *Deciduous broad leaf*, both *Closed* (114) and *Open* (124) as well  
332 as *Closed forest, mixed* (115) and *Forest, not matching any of the other definitions* (116 and  
333 126). As for the climate classification, a *One Hot Encoding* procedure was applied to landcover  
334 classes.

### 335 3.3. Point sampling

336 In the study area, the vegetated landcover classes defined above account for 96% of the total  
337 landcover, with the classes *Shrubs* (38%), *Sparse* (26%) and *Herbaceous* (17%) dominating the  
338 total count. The *Forest* class (17%) dominates the Andean part of the study area whereas crops  
339 represent about 1% of the region. 5000 instances were randomly sampled for each landcover  
340 class. The target variables and covariates for all points were downloaded from GEE and stored  
341 as a *GeoPanda* dataframe in Python.



### 342 **3.4. Setting up the machine learning model**

343 We developed an interpretable ML model able to process big EO data to identify the most  
344 important variables and how they interact to cause the impact on vegetation. This amounts to a  
345 (supervised learning) regression task; the EO data, for training and testing, include the  
346 environmental, atmospheric, and geophysical features described above, as well as the target  
347 variables consisting in the impact metrics. The main objective is to investigate and describe the  
348 nature of the processes, performing out-of-sample predictions is outside of the scope of this  
349 paper. This section introduces the ML algorithm, its optimisation and its interpretation  
350 processes. All computations are performed using *Python 3.9* on the *Gekko* cluster of NTU's  
351 *Asian School of the Environment*, both using CPUs and GPUs.

#### 352 *3.4.1. ML algorithm*

353 The main modelling challenge is to approximate complex functions mapping both  $minV$  and  
354  $minT$  to the various investigated features. Decision trees and related methods form a general  
355 class of models suitable for such regression tasks. We opt for Gradient Boosted trees, a category  
356 of decision trees that use an ensemble of so-called weak learners built sequentially to improve  
357 prediction accuracy (Müller and Guido, 2015). Gradient Boosted trees have successfully been  
358 applied on EO problems (e.g., Hengl et al., 2017). Here, we used the *XGBoost v.1.4.2* library,  
359 which provides an optimised and distributed implementation of gradient boosted trees (Chen  
360 and Guestrin, 2016).

#### 361 *3.4.2. Hyperparameter optimisation*

362 Gradient-Boosted trees rely on a range of hyperparameters governing the model's bias-variance  
363 trade-off. Selected hyperparameters (Section 4.4.1) were tuned by minimising the out-of-  
364 sample mean absolute error (MAE) computed through a 5-fold cross-validation scheme using  
365 *Scikit-learn's RepeatedKfold* and 10,000 trees. We used the *Optuna* library (Akiba et al., 2019)  
366 optimised on a single GPU.





367 3.4.3. *Model interpretation*

368 Gradient-Boosted trees can accommodate non-linear effects and interactions but, as for many  
369 modern ML algorithms, come at the cost of limited interpretability. Model-agnostic  
370 interpretation methods shedding light on black-box models are actively being developed and,  
371 when applied on big EO data, provide a novel framework to identify and constrain the processes  
372 driving changes through time in Earth Sciences (Batunacun et al., 2021; He et al., 2020; Sulova  
373 and Arsanjani, 2021). Amongst these, the Shapley additive explanations (SHAP) method of  
374 Lundberg et al., (2020), based on Shapley values (Shapley, 1956) and coalitional game theory,  
375 decomposes any prediction from a given model as a sum of the individual effects from each  
376 variable (Molnar, 2021). The method computes SHAP values, which quantify how a given  
377 feature act to change a model's mean prediction. We use here SHAP values to identify drivers  
378 of vegetation vulnerability in two ways. Firstly, the mean absolute SHAP value of a variable  
379 across all instances indicates a relative importance amongst all features. Secondly, individual  
380 SHAP values for a given feature and all instances provide insights into how a feature's value  
381 influences predictions. As generalisation is not the main objective of this study, SHAP values  
382 are computed on the full dataset. We use the *TreeExplainer* method of the SHAP library  
383 (Lundberg et al., 2020) to explain XGBoost's prediction.

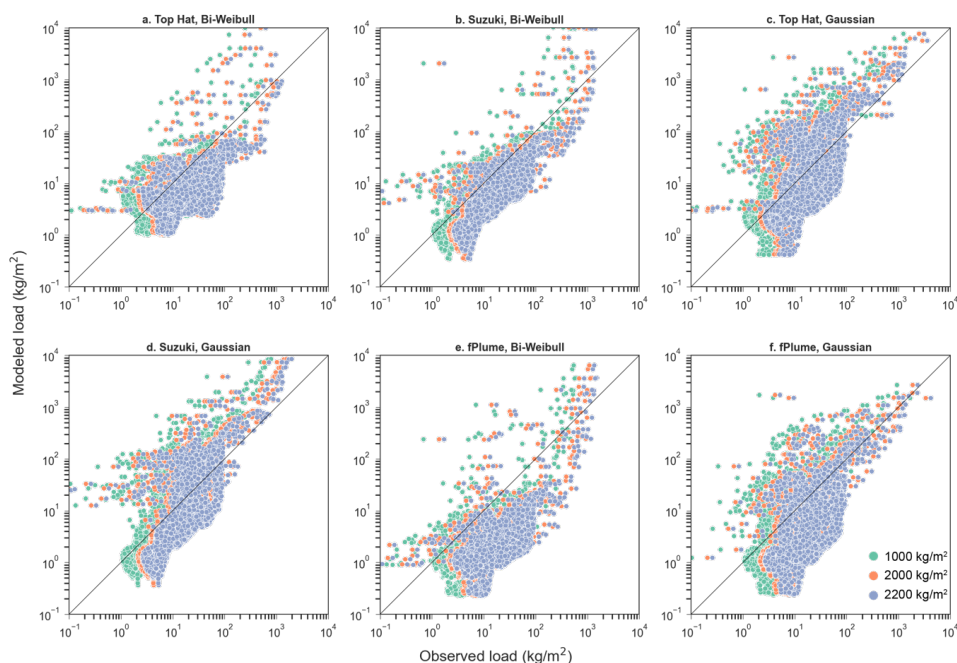
384 Unlike SHAP values, *permutation feature importance* ranks features based on their direct  
385 impact on model performance (Breiman, 2001; Fisher et al., 2019). We use it as a  
386 complementary approach to SHAP values. Permutation importance is also computed on the full  
387 dataset using *Scikit-learn's permutation\_importance* function using 10 permutations of each  
388 variable and computing the change in the coefficient of determination  $R^2$ .



389 3.4.4. Modeling scheme

390 A model is trained separately for each landcover class defined in Section 3.3, with one  
391 additional model trained on all landcover classes jointly and using the landcover class as a  
392 feature. Since *XGBoost* does not support multi-output regressions, each dataset is used as an  
393 input for two models trained using either *minV* or *minT* as a target variable (**Figure 3**). To  
394 include some dependence between the two impact metrics, the model predicting *minV* is trained  
395 with *minT* removed from the features, whereas the model predicting *minT* is trained with *minV*  
396 in the list of features.

397 **4. Results**



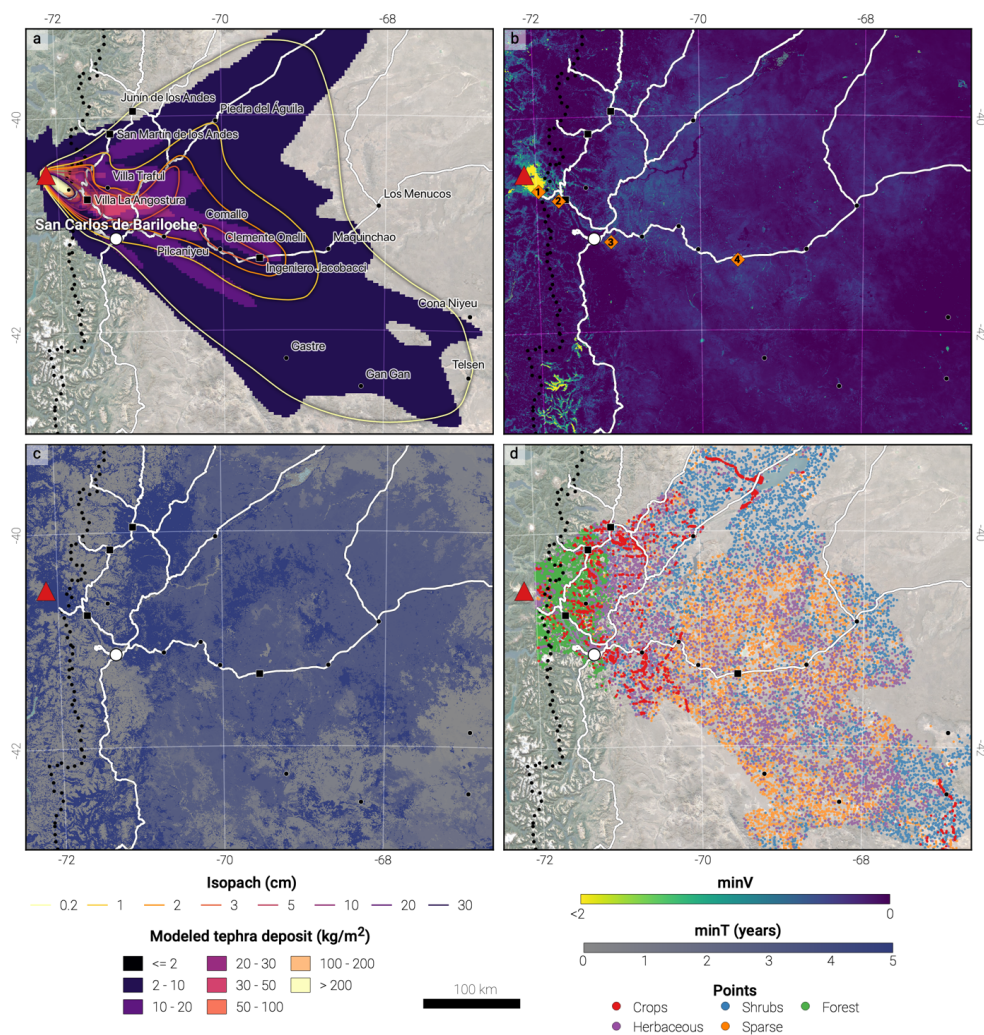
398

399 **Figure 4** : Relationship between the tephra accumulation modelled with Fall3d and inferred from isopach for the  
400 various modelling schemes (**Table 3**). Colours consider various densities used to convert deposit thickness to mass  
401 loads. Figure sub-labels follow **Table 3**. The black line shows a hypothetical 1:1 relationship.



402 **4.1. Deposit reconstruction**

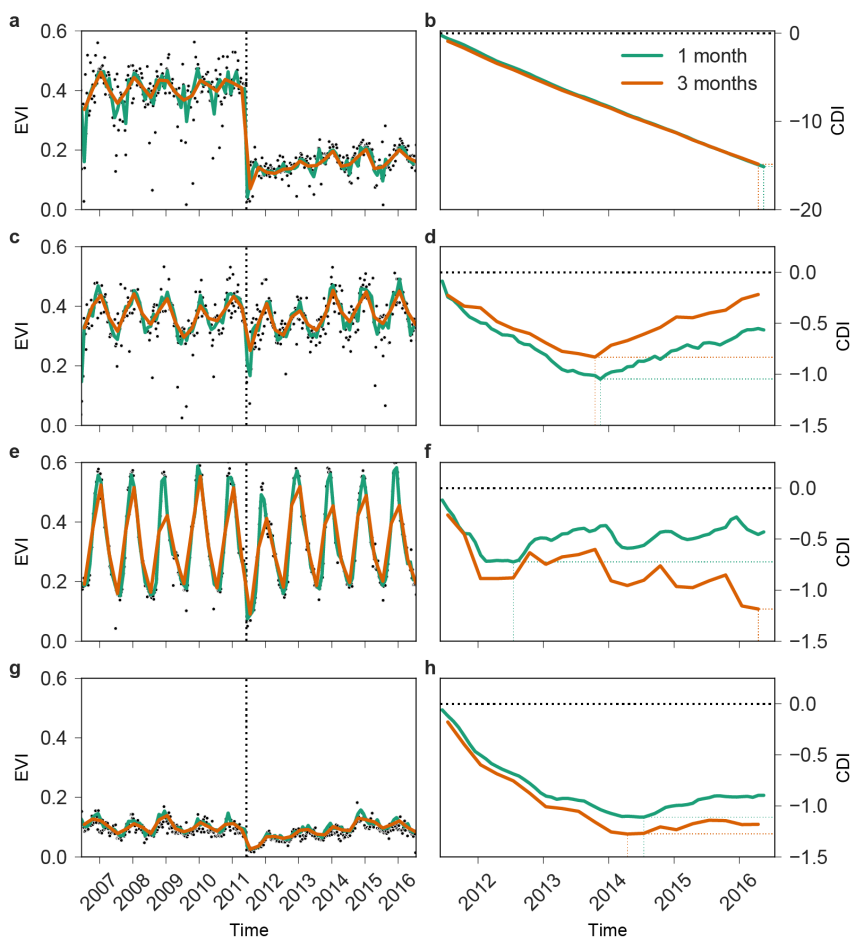
403 To select the best Fall3d run shown in **Table 3**, 10,000 points were randomly sampled in space  
404 and used to retrieve both the modelled tephra load and the thickness obtained from interpolated  
405 isopach (**Figure 4**). Although all model runs are capturing the general trend, mismatches can  
406 be attributed to modelling issues (e.g., limitation in describing sedimentation from the plume  
407 margin or aggregation processes; Bagheri et al., 2016; Poulidis et al., 2021) and isopach  
408 interpolation using a bulk density. In the perspective of these limitations, we adopted run *b* (i.e.,  
409 Suzuki plume model with a bi-Weibull grain-size distribution; **Table 3**) as it generally shows a  
410 minimum spread across the 1:1 line and provides a conservative scenario (**Figure 4**). **Figure 5**  
411 a compares the modelled load for the selected run with the isopach. The model captures both  
412 the general extend of the deposit as well as the various lobes generated as a function of variable  
413 wind conditions throughout the eruptive phase.



414

415 **Figure 5** : a Modelled load using Fall3d run b (kg/m<sup>2</sup>; **Table 3**) overlain with isopach (cm). b Spatial distribution  
 416 of *minV*. Numbered orange diamonds are referenced in the text. c Spatial distribution of *minT*. d Dataset of points  
 417 sampled in GEE coloured by their landcover class. When not specified, legend items follow Figure 1. Background  
 418 is © Google Map 2022.

419



420

421 **Figure 6** : Time series of EVI (a, c, e, g) and monthly CDI (b, d, f, h) for the four points described in Section 4.2  
 422 and located in **Figure 5**. Black dots are raw (i.e., non-composited) MODIS data whereas green and orange lines  
 423 are composited collections using a kernel of 1 and 3 months, respectively, as described in Section 3.1. On the left  
 424 plots, the vertical black dashed line indicates eruption time. On the right plots, the horizontal black dashed line  
 425 indicates a neutral budget (**Figure 3**). Coloured dotted lines indicate the location of  $minV$  and  $minT$ .

## 426 4.2. Anomaly quantification

427 **Figure 6** shows an illustration of time series of EVI and associated monthly CDI for four  
 428 representative points in the study area (**Figure 5 b**) chosen to represent the spread in tephra  
 429 accumulation and vegetation/climate types, and using compositing windows of 1 (green) and 3  
 430 (orange) months. Seasonal EVI patterns, with high values in the summer reflecting active



431 growth and low values in the winter reflecting plant dormancy, indicate that the eruption  
432 occurred during a period of low growth (Elissondo et al., 2016). Point 1 (**Figure 6 a, b**), located  
433 23 km southeast of the vent, is characterized by herbaceous vegetation and a modelled tephra  
434 load of  $330 \text{ kg/m}^2$  (thicknesses of 165–330 mm when converted with deposit densities of 2000  
435 and  $1000 \text{ kg/m}^3$ , respectively). The sharp drop in EVI after the eruption and the following  
436 persistent lower values compared to the pre-eruption baseline translate into a CDI profile  
437 showing a negative slope, which indicates that the system did not return to pre-eruptive  
438 conditions. This observation agrees with existing DDS (**Table 1**), where accumulations  $\geq 150$   
439 mm result in substantial vegetation destruction. Point 2, located 45 km southeast of the vent  
440 and 7 km from Villa La Angostura consists of closed, evergreen broadleaf forest. With  $40 \text{ kg/m}^2$   
441 of tephra accumulation (thickness of 20–40 mm for the same densities as Point 1), EVI values  
442 show a slight decrease compared to pre-eruption conditions lasting for a couple of years, after  
443 which a general trend is observed leading to larger EVI values than the baseline (**Figure 6 c**).  
444 This translates into CDI profiles showing a negative trend for two years after the eruption, after  
445 which a positive trend indicates better conditions compared to the baseline (**Figure 6 d**). When  
446 compared to existing DDS for forestry (**Table 1**), the modelled thickness spans damage classes  
447 0–3, ranging from no impact to minor productivity loss. Point 3 is 112 km from the vent in the  
448 vicinity of San Carlos de Bariloche. Classified as crops by the CGLS landcover and looking  
449 like pastoral grazing fields from high resolution satellite imagery, it was affected by  $7 \text{ kg/m}^2$  of  
450 tephra (thickness of 3.5–7 mm; damage classes 0–3; **Table 1**). Both compositing time windows  
451 show a reduction in EVI values for at least one season after the eruption, which translates to a  
452 local CDI minimum about a year after the eruption (**Figure 6 e, f**). Finally, Point 4 is located  
453 240 km southeast of the vent close to Ingeniero Jacobbaci and was affected by  $10 \text{ kg/m}^2$  of  
454 tephra (i.e. 5–10 mm). Classified as herbaceous vegetation in the CGLS dataset but looking like  
455 farmland with a mixture of pasture and crops on high-resolution satellite imagery, both EVI



456 and CDI profiles indicate a return to pre-eruption conditions after ~3 years, after which a  
457 positive CDI slope indicates temporary better conditions (**Figure 6 g, h**).

458 **Figure 6** illustrates the differences in quantifying  $minV$  and  $minT$  when using time windows of  
459 1 and 3 months in Equation 1. A 1-month window closely follows local trends and results in  
460 irregular CDI curves, whereas a 3-months window over-smooths local variations. Although  
461 both approaches commonly result in similar results, Point 3 illustrates how the two windows  
462 can induce different interpretations. We adopt a 3-months kernel for two main reasons. Firstly,  
463 the visual comparison of the spatial distribution of  $minV$  and  $minT$  on a map shows that such  
464 differences occur locally whilst preserving the general spatial distribution. Secondly, points  
465 displayed in **Figure 6** are not heavily affected by cloud coverage, and the 1-month kernel does  
466 not reflect the typical effects that clouds can induce when using such a small compositing time  
467 window (e.g., sparse time-series, artefacts, etc.). This is generally not the case, either around  
468 Cordon Caulle volcano where the region closer to the vent suffers too much cloud coverage to  
469 be resolved by a 1-month kernel, or around most volcanoes around the world where large and  
470 high edifices are often cloudy. Therefore, the 3-months kernel provides a more conservative  
471 approach and enables reproducibility to other case studies.

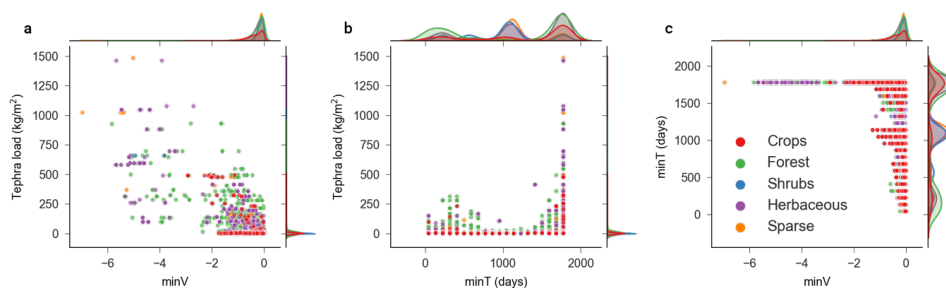
### 472 **4.3. Impact mapping**

473 **Figure 5 b** displays the spatial distribution of  $minV$  in the study area. The region with the  
474 minimum  $minV$  value extends up to 25 km southeast of the vent and corresponds to  
475 accumulations of ~550 kg/m<sup>2</sup>. Although conspicuous, it is impossible to unequivocally attribute  
476 this impact to tephra fallout in proximal area where other hazards can occur (e.g., pyroclastic  
477 density currents, lahars). Except for this region, the impact within the first 80 km east of the  
478 vent is relatively limited, beyond which a sharp, north-south oriented decrease in  $minV$  values  
479 occur. This rapid change corresponds to a change in rainfall amount, a transition from well-



480 developed andosols to very weakly-developed regosols and a region dominated by forests to  
481 one dominated by shrubs and herbaceous vegetation (Figure 1; Section 2.2). In this region,  
482 minimum  $minV$  values are  $\sim -0.5$  and the spatial distribution of  $minV$  reflects the spatial  
483 distribution of tephra fallout. Negative  $minV$  values extend eastwards beyond the town of Los  
484 Menucos, suggesting that impact occurred with accumulations  $\leq 2$  kg/m<sup>2</sup>. Due to the use of a 3-  
485 months kernel,  $minT$  is a discrete rather than a continuous dataset (i.e., a  $minT$  value of 4.5  
486 months suggests that  $minV$  was reached between 3–6 months after eruption onset). The spatial  
487 distribution of  $minT$  (Figure 5 c) generally reflects  $minV$  and the pattern of tephra accumulation.  
488 Note that artefacts related to non-vegetated areas are ignored (e.g., bare rock and snow-covered  
489 mountains in the S).

490 **Figure 5 d** shows the distribution of sampled points by landcover and selected relationships are  
491 plotted in **Figure 7**. Although **Figure 7 a** displays a general negative relationship between  $minV$   
492 and the tephra load, a simple linear relationship fails to accurately capture the variability of  
493 impact. For  $minT$ , **Figure 7 b** and c show how  $minT$  is distributed around three main modes of  
494 tephra load and  $minV$ . Landcover classes that are most impacted by long  $minT$  values are Forests  
495 and Herbaceous, which are the two classes the most exposed to heavy loads (**Figure 5**). Plotting  
496  $minT$  shows a distribution centred around three modes of about 400, 1000 and 1700 days  
497 (**Figure 7 b**). No clear relationship appears between  $minT$  and either  $minV$  or tephra load.



498





499 **Figure 7** : Relationship between **a**  $minV$  and the total tephra load, **b**  $minT$  and the total tephra load and **c**  $minV$  and  
500  $minT$  as a function of the landcover class. The marginal axes contain a kernel density estimate of the underlying  
501 population for each landcover class. For readability all forest sub-groups are grouped.

#### 502 **4.4. ML model**

503 **Table 4** : Summary of the trained models. The *Optimisation* columns group reports the hyperparameter values  
504 obtained with the optimisation process. The *Model metrics* columns group reports the mean absolute error (MAE)  
505 and the  $r^2$  coefficients on both training and test datasets. The mean and the standard deviation (Std) were obtained  
506 by 5-fold cross validation with three repeats.

##### 507 *4.4.1. Model performance*

508 **Table 4** presents the results of the optimization of hyperparameters on the dataset shown in  
509 **Figure 5 d** and the associated model metrics. Hyperparameters for all model runs generally  
510 showed a balance between parameters indicating a more (i.e., high values of alpha, lambda and  
511 min child weight) or less (i.e., high values of max depth and learning rate) conservative model.  
512 The MAE and  $R^2$  were computed on both training and testing datasets using a cross-validation  
513 with five folds and three repeats. We compare training and testing prediction error as an  
514 indication of the degree of overfitting of the model. As expected, model metrics obtained on  
515 test datasets were lower than those using training data. Based on the  $R^2$  of the testing data and  
516  $minV$ , models trained on all landcover classes and on herbaceous vegetation performed well  
517 ( $R^2 > 0.9$ ), followed by forests ( $R^2 > 0.8$ ) and crops ( $R^2 > 0.7$ ). The particularly low  $R^2$  value for  
518 sparse vegetation can be attributed to the presence of <10% vegetated cover in this class, which  
519 is dominated by bare soil or rock. The  $R^2$  values of  $minT$  are consistently lower than those for  
520  $minV$  and never exceed 0.6, which we partly attribute to its discrete nature.

521 Overall, the comparison of error metrics between testing and training sets reveal that models  
522 trained on the various datasets have various degrees of generalisation ability, with the caveat  
523 that the validity of the insights provided by the different models should be considered in the  
524 perspective of their respective performances. The broadest dataset considering all landcover



525 classes and  $minV$  results in high training (0.94) and testing (0.91)  $R^2$  values. We use this good  
526 performance and similarity between both values as an indication that the model is likely not  
527 overfitting and yields good generalisation.

528 **Table 5** : Ranking of feature importance computed using mean absolute SHAP values and permutation importance  
529 for all landcover class and impact metrics. A darker cell colour indicates a stronger importance. For each column,  
530 the 3 most important features are in bold and the 10 most important features are in red.

#### 531 4.4.2. Feature importance

532 **Table 5** summarizes feature importance for each landcover class using the mean absolute SHAP  
533 value and permutation importance. Although some differences exist, both methods yield similar  
534 results, thus implying that features that contribute the most to predictions (SHAP importance)  
535 also improve the model's generalization error (permutation importance). Unless specified, this  
536 section focuses on SHAP importance.

537 *EVI* and *elevation* are the two features that consistently rank in the top 10 of the most important  
538 variables across impact and landcover. For  $minT$ ,  $minV$  is the most important variable, which  
539 suggests that both impact metrics are dependent. *EVI* ranks especially high, which indicates  
540 that the mean *EVI* value computed over the year before the eruption provides an important  
541 background level to the model. The variable *Lapilli* is the most important for  $minV$  for all  
542 landcover classes but crops (SHAP value) and sparse (permutation importance) and ranks high  
543 when predicting  $minT$  for all and the forest landcover classes.

544 For forests,  $minV$  is best predicted, in decreasing order, by *lapilli*, *EVI* and *elevation*, which are  
545 respectively a deposit, a proxy for a biotic and an abiotic parameter. Note that using permutation  
546 importance instead of SHAP importance suggests that the 3<sup>rd</sup> most important variable is surface  
547 temperature, which is correlated to elevation. In parallel,  $minT$  is driven by  $minV$ , *lapilli*,  
548 elevation and *EVI*, which indicates that the duration of impact is dominantly proportional to the  
549 magnitude of impact and the tephra load, with additional biotic and abiotic controls. This



550 suggests that forests are potentially more resilient to moderate accumulations of ash and might  
551 rather be prone to direct, physical impact from heavy accumulations. In comparison, the *minV*  
552 of herbaceous vegetation is controlled by lapilli, EVI and the 6-months precipitation, which  
553 indicates the same hierarchy of importance of deposit, biotic and abiotic parameters as for  
554 forests, whereas *minT* is controlled by *minV*, EVI, the 3-months precipitation and fine ash.  
555 Interestingly, this suggests that impact duration does not primarily depend on any deposit  
556 variable, the most important of which (i.e., fine ash) is different to the parameter controlling the  
557 magnitude of impact (i.e., lapilli). As a final example, no deposit property ranks in the top 3  
558 variables controlling the *minV* values of crops, which include climate, EVI and the 3-months  
559 precipitation anomaly. The first deposit parameter, fine ash, ranks 4<sup>th</sup>, which indicates that the  
560 vulnerability of crops to ash fallout is dominantly constrained by biotic and abiotic parameters.  
561 Fine ash ranks 5<sup>th</sup> for *minT*, which is mainly driven by *minV*, EVI and the slope, and illustrate  
562 how abiotic parameters can potentially dominantly control impact magnitude and duration.

#### 563 4.4.3. SHAP dependence plots

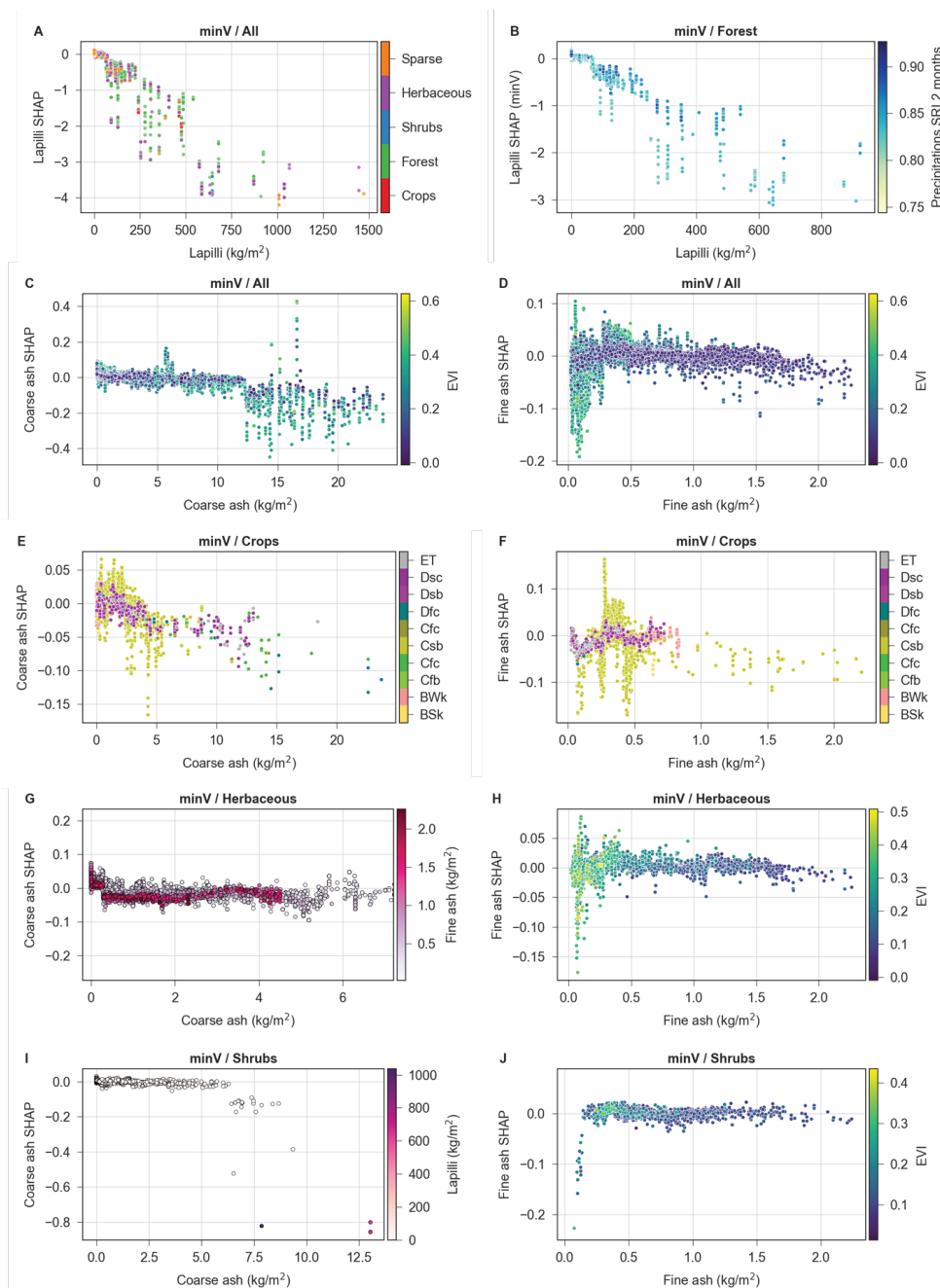
564 SHAP dependence plots (Fig. 8) display, for each instance in the dataset (i.e., a point in **Figure**  
565 **5 d**), the SHAP value of a given variable as a function of its actual value. For a given instance  
566 and a given variable, a negative SHAP values implies that the variable contributed to reducing  
567 the predicted value compared to the mean prediction of the model. Therefore, a negative SHAP  
568 value for *minV* implies a contribution to *increase* the magnitude of impact, whereas a negative  
569 SHAP value for *minT* implies a contribution to *decrease* the duration of impact.

#### 570 **Impact of deposit on *minV* predictions**

571 **Figure 8 a** is the dependence plots for lapilli. With loads  $\leq 60$  kg/m<sup>2</sup> of lapilli, SHAP values  
572 are contained within  $0 \pm 0.1$ , but drastically drop for larger loads. Lapilli being dominantly  
573 impacting the vicinity of the volcanic source, <4% of all instances are affected by  
574 accumulations  $>60$  kg/m<sup>2</sup> with those areas dominantly consisting of forests with additional



575 vegetation classified as shrubs and herbaceous (Figure 1 c). Despite limited points, **Figure 8 a**  
576 suggests stepwise decreases in SHAP values for lapilli loads of ~60, 230 and 550 kg/m<sup>2</sup>. Using  
577 a deposit density of 1000 kg/m<sup>3</sup>, thicknesses of 60, 230 and 550 mm span the D1–D4 damage  
578 states for forestry (Jenkins et al., 2014; Table 1). Using the pastoral class of Table 1 as an  
579 analogue for shrubs and herbaceous vegetation, these accumulations suggest that, for crops,  
580 substantial to major land rehabilitation is required before recovery. These observations confirm  
581 the relationships between *minV*, *minT* and the deposit load shown in Figure 7: points affected  
582 by high lapilli loads result in *minT* values larger than ~1300 days and an impact that persisted  
583 for years after the eruption. These high impact metrics explain why lapilli is the most important  
584 variable to predict *minV*. Lapilli is likely to cause a direct, physical impact from the high kinetic  
585 energies (e.g., Blake et al., 2015; Osman et al., 2019), breakage from a static load and burial  
586 (Arnalds, 2013; Ayris and Delmelle, 2012), which is captured as a strong anomaly by our  
587 method and results as the most important variable. Plotting the dependence plot of lapilli for  
588 the model trained on the generic forest landcover class (**Figure 8 b**) indicates that the 2-months  
589 precipitation anomaly contributes to further explaining the influence on the SHAP value, with  
590 points with an anomaly <0.85 displaying lower SHAP values.



591

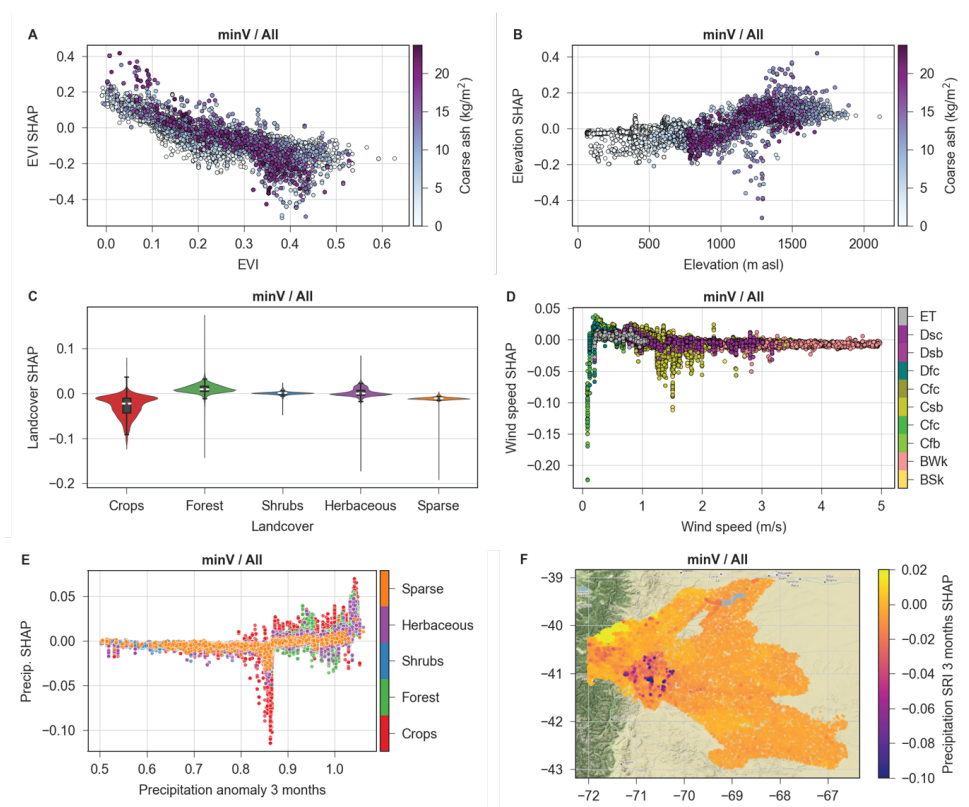
592 **Figure 8:** SHAP dependence plots illustrating the effect of deposit on the  $minV$  value predicted by the models for  
593 **a** lapilli using all landcover classes, **b** lapilli on the forest subclass and **c-j** coarse and fine ash for selected landcover  
594 classes. The hue of the points is related to additional explanatory variables. For **a**, **e** and **f**, the colour scheme  
595 follows Figure 1. Negative SHAP values contribute to decreasing  $minV$  and therefore increase impact.



596 Dependence plots for coarse and fine ash (**Figure 8 c, d**) display similar – although less  
597 conspicuous – drops in SHAP values for accumulations of 12 and 1.7 kg/m<sup>2</sup>, respectively, with  
598 SHAP values on average one order of magnitude smaller than for lapilli. Considering that fine  
599 deposits are denser than coarser ones, a density range of 1000–2000 results in thicknesses of 6–  
600 12 and 0.9–1.7 mm for coarse and fine ash, respectively, which cover the D1–D3 damage  
601 classes for Horticultural/Arable and Pastoral agriculture (**Table 1**). Note that these thicknesses  
602 should be regarded as minimum values as we convert here individual size fractions to total  
603 deposit thickness. **Figure 8 e–j** also shows the effect of ash for models trained on specific  
604 landcover classes. For crops (**Figure 8 e–f**), coarse and fine ash are the 10<sup>th</sup> and the 4<sup>th</sup> most  
605 important variables, respectively. Coarse ash induces significant drops in SHAP values for  
606 loads of 2, 4 and 10 kg/m<sup>2</sup>. There is clearly an effect of fine ash on SHAP values but the  
607 oscillatory pattern is difficult to explain for loads  $\leq 0.5$  kg/m<sup>2</sup>, especially for the Csb climate  
608 class where most crops are found (i.e., Warm temperate, summer dry, warm summer), and  
609 probably depends on additional variables not accounted for in the model (e.g., geographic  
610 distribution of plant-specific effects such as ash retention as a function of leaf morphology).  
611 Beyond 1 kg/m<sup>2</sup>, SHAP values are consistently negative. Coarse and fine ash are the 4<sup>th</sup> and the  
612 14<sup>th</sup> most important variables for *minV* for herbaceous vegetation. The coarse ash shows more  
613 negative SHAP values when associated with fine ash. Fine ash is generally beneficial for  
614 herbaceous vegetation with low EVI values (**Figure 8 h**). The most negative SHAP values are  
615 found for high-EVI herbaceous vegetation for accumulations  $\leq 1$  kg/m<sup>2</sup> and show both positive  
616 and negative behaviours. Since no co-variate satisfactorily explains this contrasting behaviour,  
617 this is either due to a model artefact or to variables that are not accounted for in the model. For  
618 shrubs (**Figure 8 i–j**), coarse and fine ash are respectively the 7<sup>th</sup> and 12<sup>th</sup> most important  
619 variables. Coarse ash shows a sharp decrease in SHAP values for loads of  $\sim 6$  kg/m<sup>2</sup>, beyond



620 which the magnitude of the negative effect increases with the lapilli load. Fine ash doesn't show  
621 any trend or sharp break.



622  
623 **Figure 9:** a–e SHAP dependence plots illustrating the effect of various variables on the prediction of *minV*. a–b  
624 Effect of EVI (a) and elevation (b) on the SHAP value as a function of the coarse ash load. c Violin plot showing  
625 the distribution of SHAP values for each landcover class with a box-and-whisker plot overlain. d Effect of wind  
626 speed on the SHAP values as a function of climate. e Effect of the 3-months precipitation anomaly on the SHAP  
627 value as a function of landcover. f Spatial distribution of 3-months precipitation anomaly SHAP values. Map tiles  
628 by Stamen Design CC BY 3.0, map data © OpenStreetMap contributors.

### 629 **Impact of other features on the prediction of *minV***

630 **Figure 9** shows SHAP dependence plots for variables other than the deposit. **Figure 9** a  
631 confirms the importance of EVI on *minV*, where all points with  $EVI < 0.1$  result in positive  
632 SHAP values and all points with  $EVI > 0.3$  result in negative SHAP values. This observation is



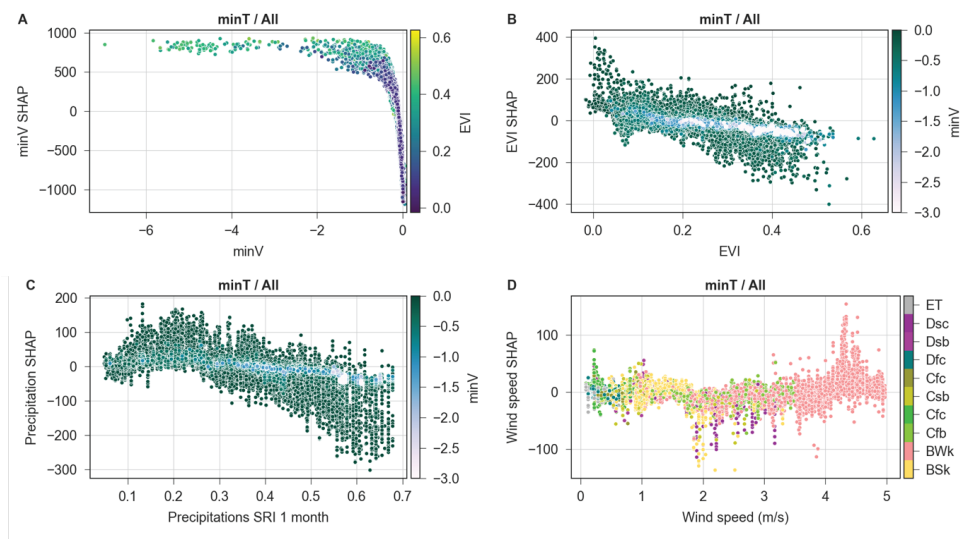
633 partly a consequence of the use of Equation 1, where the value of  $VI_{ijk} - \overline{VI_{ij}}$  is generally larger  
634 for higher EVI values. **Figure 9** a also suggest a dependence of this relationship on the load of  
635 coarse ash, which slightly increases SHAP values for low EVI, but decreases them for higher  
636 values. Elevation is the 3<sup>rd</sup> important feature for predicting  $minV$  and shows a breakpoint at an  
637 altitude of ~1000 m asl (**Figure 9** b), below which SHAP values are dominantly negative.  
638 Above this elevation, SHAP values are generally positive, regardless of the intensity of ash  
639 accumulation. Landcover, the 7<sup>th</sup> most important feature, indicates that crops dominantly  
640 contribute to increasing impact in the model (**Figure 9** c). Sparse vegetation also has a negative  
641 but less pronounced effect on SHAP values, whereas shrubs and herbaceous vegetations have  
642 a neutral effect. The SHAP values of forests tend to reduce the impact, which corroborates the  
643 higher resilience of trees to tephra fallout (**Table 1**).

644 Wind and precipitation partly control the residence time of ash on leaves and therefore the  
645 impact (Ayrís and Delmelle, 2012). Although variables used here only consider pre-eruption  
646 atmospheric conditions, they are indirectly used as indicators for post-eruption patterns. The  
647 impact of wind speeds on SHAP values shows breakpoints at 0.2 and 1.2 m/s. SHAP values are  
648 strongly negative below 0.2 m/s, generally positive up to 1.2 m/s and generally negative above  
649 (**Figure 9** d). This supports the idea that wind contributes to reducing the residence time of ash  
650 on leaves, but the aeolian remobilization of ash at higher wind speeds can negatively impact  
651 vegetation (e.g., Arnalds, 2013; Craig et al., 2016b; Elissondo et al., 2016; Wilson et al., 2011).  
652 Although depending on additional parameters (e.g., surface roughness, ash properties, soil  
653 humidity, rainfall intensity), an empirical value for onset of remobilization of 0.4 m/s has been  
654 used in the literature and agrees with our results (e.g., Folch et al., 2014; Liu et al., 2014).  
655 Leadbetter et al., (2012) observed that ash resuspension is suppressed if precipitation rates  
656 exceed 0.01 mm/h, and our model indicates that most negative SHAP values occur for relatively  
657 dry climates. The most important precipitation variable for predicting  $minV$  with all landcover





658 classes is the precipitation anomaly computed over 3 months before the eruption, which mostly  
659 shows a negative anomaly (i.e., anomaly < 1; Table 5; **Figure 9 e**). This precipitation anomaly  
660 shows a clear break at a value of 0.87, for which SHAP values are dominantly negative below  
661 and positive above. Above a value of 1, SHAP values increase. **Figure 9 e** shows a negative  
662 peak in SHAP values between an anomaly of 0.85–0.87 across all landcover classes but stronger  
663 for crops. Plotting SHAP values on a map (**Figure 9 f**), the spatial clustering of negative SHAP  
664 values corresponds to the location of crops between San Carlos de Bariloche and Comallo  
665 (**Figure 1**). No variable unequivocally explains this spatial clustering.



666  
667 Figure 10: SHAP dependence plots for *minT* showing the effect on the SHAP value from **a** *minV* as a function of  
668 EVI; **b** EVI as a function of *minV*; **c** 1-month precipitation anomaly as a function of *minV* and **d** wind speed as a  
669 function of climate. Negative SHAP values contribute to decreasing *minT* and therefore decrease impact the  
670 duration for reaching *minV*.

### 671 Features driving *minT*

672 With a mean absolute SHAP value >7 times larger than any other variable, *minV* is by far the  
673 most important for predicting *minT* (Figure 10 a), with a cut-off between positive (i.e.,  
674 increasing the value of *minT*) and negative (i.e., decreasing *minT*) at a *minV* value of ~0.15. The



675 effect of EVI on  $minT$  is the opposite of  $minV$  (**Figure 9 a**): although high EVI values tend to  
676 increase the impact magnitude (lower  $minV$ ), they generally contribute to reducing the impact  
677 duration (i.e., **Figure 10 b**). Interestingly, this trend disappears as  $minV$  increases. This can be  
678 explained by the fact that points affected by high  $minV$  values in **Figure 10 b** are associated with  
679 relatively high  $minT$  values (**Figure 7**; **Figure 10 a**). These points are associated with damage  
680 classes suggesting land retirement, and their recovery is therefore independent of the pre-  
681 eruption EVI level. The 1-month precipitation anomaly is the 5<sup>th</sup> most important variable for  
682  $minT$  (**Figure 10 c**), and SHAP values are mostly positive below an anomaly of 0.3 and mostly  
683 negative above 0.5. As for EVI, high  $minV$  values are less sensitive to the general trend. Finally,  
684 **Figure 10 d** shows the effect of the wind speed at the time of eruption on  $minT$  as a function of  
685 the climate. Wind speeds  $>4$  m/s considerably increase  $minT$ , especially in an arid climate (i.e.,  
686 BWk) where the vegetation is mostly shrubs, herbaceous and sparse. Points with positive SHAP  
687 values at wind speeds  $>4$  m/s are characterized by accumulations of fine ash  $>0.5$  kg/m<sup>2</sup>. In  
688 contrast, points with minimum SHAP values between wind speeds of 1.8–2.8 m/s correspond  
689 to crops close to Piedra del Aguila and show fine ash loads  $<0.5$  kg/m<sup>2</sup>.

## 690 **5. Discussion and perspectives**

691 The proposed methodology provides a new framework to systematically assess the vulnerability  
692 of vegetation to tephra fallout as a dynamic, multi-variate problem. Its application to the CC  
693 2011 eruption highlights how big EO datasets and interpretable machine learning could help  
694 acquiring a new knowledge from tens to hundreds of understudied eruptions recorded in  
695 archives of multispectral images. This approach aligns with FAO's objective of gaining a global  
696 understanding of vegetation vulnerability through the systematic study of their impacts and, in  
697 turn, contributes to various Sustainable Development Goals (SDGs 2.4, 13.1, 15.3). Specific to  
698 volcanic risk, this is the first effort to provide a large scale, quantitative basis to estimate the



699 impacts of explosive volcanic eruptions on food production. On a longer time-scale and large  
700 spatial scale, this is the first step towards tackling the unaddressed *black elephant* event that is  
701 the risk of future large eruptions on food security (Lin et al., 2021).

#### 702 **Validation and causal inference of impact mechanisms**

703 Our methodology focuses on impact mechanisms either occurring from the direct action or  
704 arising from interactions between physical properties. Since we neglect the impact from water  
705 leachable elements (e.g., Stewart et al., 2020), the approach is more suited to dominantly  
706 magmatic events rather than eruptions with a significant hydrothermal component. Impact  
707 patterns captured by our methodology are corroborated by lessons learned from empirical post-  
708 EIA and experiments. For CC 2011, the model suggests that, except for points subjected to  
709 destruction from large tephra loads, various biotic and abiotic variables tend to have a more  
710 critical control on both impact magnitude and impact duration than deposit properties (**Table**  
711 **5**). SHAP dependence plots for deposit properties (e.g., **Figure 8 a–e**) identify similar tephra  
712 thresholds as those identified in existing DDS (**Table 1**). Nevertheless, recent findings from  
713 size distribution, ranging from physical impact for large lapilli to a reduction of light  
714 interception from fine ash leading to a decrease in photosynthesis (e.g., Ligot et al., submitted;  
715 Ligot et al., in prep). DDS must therefore consider other hazard impact metrics than only tephra  
716 thickness, and Fig. 8–10 are the first attempt towards this objective. The method is also able to  
717 capture impacts arising from interaction between other parameters than deposit properties. For  
718 instance, **Figure 9 d** suggests that the model captures the general relationship between presence  
719 of ash, precipitation (inferred from climate) and wind speed in controlling the impact from  
720 aeolian remobilisation. This demonstrates the ability of the model to identify complex and  
721 dynamic processes, and cross-validating thresholds inferred from the model with values from  
722 existing post-EIA and experiments provides a systematic framework to generalize observations



723 made at different scales (Dominguez et al., 2020a; Forte et al., 2017; Leadbetter et al., 2012;  
724 Liu et al., 2014).

725 Despite these observations, methodologies for interpretable ML should be carefully used when  
726 attempting to infer causality from correlations/associations. Suggestions of causality are  
727 currently restricted to effects that rely on phenomena that have been either witnessed in the field  
728 or experiments. Other variables considered in our dataset show conspicuous and complex  
729 patterns that we are unable to explain (e.g., **Figure 8 f**, **Figure 9 e**). Such patterns have two  
730 possible explanations (or a combination of both): either the model fails to accurately capture  
731 the underlying relationship between feature and target variable, or the relationship is  
732 complicated by other factors (e.g., feature interactions, confounding variables), including  
733 unobserved ones. Investigating which association captures true causality therefore requires the  
734 development of synergies between various relevant disciplines (e.g., physical volcanology,  
735 ecology, soil sciences, disaster risk reduction). The development and adaptation of existing  
736 causal inference methods in Earth Sciences to investigate a system's causal interdependencies  
737 is an active topic of research (Runge et al., 2019).

#### 738 **Towards a model for agricultural crops and food production**

739 The methodology currently relies on the CGLS-LC100 land cover dataset do distinguish  
740 between natural vegetation and agriculture. We focus here on agricultural crops which, despite  
741 representing ~1% of the study area, show the highest vulnerability to tephra fall (**Figure 9**).  
742 Note that although pastoral crops are included in the *Herbaceous vegetation* class in CGLS-  
743 LC100, it is impossible to distinguish between natural and managed grassland (Buchhorn et al.,  
744 2020). Post-EIA on agricultural impacts have demonstrated how agriculture vulnerability  
745 depends on various factors that are not included in our model, including some of socio-  
746 economic nature (Blake et al., 2015; Magill et al., 2013; Phillips et al., 2019; Wilson et al.,  
747 2013, 2007; Ligot et al., submitted) that reflect specific challenges associated with different



748 farming activities (e.g., pastoral versus horticultural, intensive versus subsistence farming).  
749 Although future evolutions of the CGLS-LC100 dataset will possibly include finer sub-  
750 definitions of the crops class (e.g., irrigated versus rainfed cropland, farm size; [Buchhorn et al.,](#)  
751 [2020](#)), the methodology currently considers all agricultural crops as a uniform system.

752 Despite this limitation, the proposed methodology nevertheless follows impact mapping  
753 techniques implemented in several other approaches for vegetation and food security mapping  
754 and monitoring (e.g., Meroni et al., 2019; Poortinga et al., 2018; Rembold et al., 2019), but  
755 differ in their fundamental purposes. To our knowledge, we provide here the first attempt to  
756 combine numerical modelling, big EO data and ML into a framework to re-analyse and extract  
757 new knowledge from data recorded in decades of remote sensing images as the basis for a new  
758 type of evidence-based vulnerability model. However, several steps are required for future  
759 evolutions of our approach to inform quantitative risk assessments on food production and  
760 security. Amongst them, future iterations of the methodology will focus on achieving:

- 761 1. More applications of the model to various types of climates, eruptions and sampling  
762 different relationship between eruption date and phenological cycle in order to improve  
763 its generalisation;
- 764 2. Comparison, validation and scaling of the EVI-based impact metrics with other impact  
765 estimates, either based on field interviews (e.g., yield loss), mapping (e.g., percentage  
766 of destroyed or damage vegetation) or other indirect proxies for physical processes (e.g.,  
767 Gross and Net Primary Productivity).

#### 768 **Caveats and future research**

769 Below are future challenges and possible improvements of the method.

- 770 1. The methodology takes advantage of datasets available on GEE (**Table 2**) and combines  
771 datasets of different nature, spatial and temporal resolutions. This discrepancy affects



772 the accuracy of the model, and future development will explore a balance between the  
773 spatial and temporal resolutions of all datasets. Specifically ERA5 data will be  
774 reanalysed using mesoscale atmospheric models (e.g., Skamarock et al., 2019) at a  
775 resolution consistent with other datasets;

776 2. An inherent and inevitable dependency exists between the various datasets; some are of  
777 ecological nature (e.g., climate is a function of precipitation and temperature) whereas  
778 other are geographic coincidences (e.g., lapilli dominantly affect the Cfb climate class,  
779 Figure 1). Further work is necessary to explore how these dependences influence model  
780 prediction and interpretability;

781 3. The methodology currently relies only on pre-eruption values for covariates. In order to  
782 capture the evolution of post-eruptive aspects (e.g., ash residence on vegetation surface  
783 as a function of wind and precipitations), future applications of the model will include  
784 post-eruption variables in the training process;

785 4. Despite providing a satisfactory accuracy, other algorithms and models than gradient  
786 boosted regression trees allowing multi-output predictions must be explored to model  
787  $minV$  and  $minT$  jointly;

788 5. ML models used in EO applications rarely accommodate spatial (and spatio-temporal)  
789 dependence. Accounting for these is necessary for reliable (causal) inference and  
790 uncertainty quantification. We plan to investigate the use of Gaussian processes, among  
791 others, to capture any residual spatial dependence.

## 792 **6. Conclusion**

793 We developed a methodology to remotely quantify impact through a combination of big EO  
794 data, interpretable ML and physical volcanology as a first step towards the development of a  
795 framework to identify, quantify and generalize key variables driving the impact of vegetation



796 after an eruption. The methodology is designed to provide a high-level and complementary  
797 perspective to dedicated studies of the various disciplines involved in the characterization of  
798 the vulnerability and impact of vegetation and crops to natural hazards, and has the potential to  
799 enhance the development of new synergies between the different actors and stakeholders  
800 involved in this specific facet of risk.

801 Based on the application of the methodology to the 2011 eruption of Cordon Caulle, the main  
802 conclusions are:

- 803 - Both the magnitude and the duration components of impact captured by the processing  
804 of MODIS satellite imagery reflect the geometry of the deposit (**Figure 5**);
- 805 - The methodology provides a systematic approach to identify the nature of the most  
806 important variables controlling the final impact metrics. The forest landcover class is  
807 mostly controlled by deposit properties (e.g., lapilli accumulation), whereas the crops  
808 landcover class predominantly depends on biotic and abiotic parameters;
- 809 - Interpretable machine learning methods provide insights into the nature of impacts. For  
810 instance, forests appear to be impacted by a direct physical impact caused by heavy  
811 accumulations;
- 812 - Across landcover classes present in the study area, SHAP dependence plots suggest that  
813 forest and crops are the most and the least resilient vegetation classes to tephra  
814 accumulation, respectively (**Figure 9 c**);
- 815 - The interpretation of SHAP dependence plots for deposit properties of the different  
816 landcover classes (**Figure 8**) are in good agreement with thresholds for existing DDS  
817 inferred from post-event impact assessments (**Table 1**), which further reinforces the  
818 validity and usefulness of our approach.



819 **Author contribution**

820 SB designed the project, elaborated the methodology and wrote the Python library with inputs  
821 from all co-authors on aspects of volcanic risk (SFJ, TW), interactions between tephra deposits  
822 and vegetation (PD) and data science (WHA). All authors contributed to the manuscript.

823 **Competing interests**

824 The authors declare that they have no conflict of interest.

825 **Acknowledgements**

826 We are grateful to Edwin Tan and EOS/ASE's HPC for support on the Gekko cluster, to Lucia  
827 Dominguez for providing isopach maps, to Jan Peuker for his patience and advice for the  
828 development of ML modelling strategies and to Oege Dijk for developing the  
829 *explainerdashboard* library. This work was supported by the National Research Foundation  
830 Singapore and the Ministry of Education—Singapore under the Research Centres of Excellence  
831 initiative (SB, SJ).

832 **References**

- 833 Akiba, T., Sano, S., Yanase, T., Ohta, T., Koyama, M., 2019. Optuna: A Next-generation  
834 Hyperparameter Optimization Framework. ArXiv190710902 Cs Stat.
- 835 Arnalds, O., 2013. The Influence of Volcanic Tephra (Ash) on Ecosystems, in: Sparks, D. (Ed.),  
836 Advances in Agronomy. Elsevier, Amsterdam, pp. 331–380.  
837 <https://doi.org/10.1016/B978-0-12-407685-3.00006-2>
- 838 Asoka, A., Mishra, V., 2015. Prediction of vegetation anomalies to improve food security and  
839 water management in India. Geophys. Res. Lett. 42, 5290–5298.  
840 <https://doi.org/10.1002/2015GL063991>
- 841 Ayris, P.M., Delmelle, P., 2012. The immediate environmental effects of tephra emission. Bull.  
842 Volcanol. 74, 1905–1936. <https://doi.org/10.1007/s00445-012-0654-5>
- 843 Bagheri, G., Rossi, E., Biass, S., Bonadonna, C., 2016. Timing and nature of volcanic particle  
844 clusters based on field and numerical investigations. J. Volcanol. Geotherm. Res. 327,  
845 520–530. <https://doi.org/10.1016/j.jvolgeores.2016.09.009>
- 846 Batunacun, Wieland, R., Lakes, T., Nendel, C., 2021. Using Shapley additive explanations to  
847 interpret extreme gradient boosting predictions of grassland degradation in Xilingol,  
848 China. Geosci. Model Dev. 14, 1493–1510. <https://doi.org/10.5194/gmd-14-1493-2021>





- 849 Beck, H.E., Zimmermann, N.E., McVicar, T.R., Vergopolan, N., Berg, A., Wood, E.F., 2018.  
850 Present and future Köppen-Geiger climate classification maps at 1-km resolution. *Sci.*  
851 *Data* 5, 180214. <https://doi.org/10.1038/sdata.2018.214>
- 852 Biass, S., Jenkins, S., Lallemand, D., Lim, T.N., Williams, G., Yun, S.-H., 2021. Remote sensing  
853 of volcanic impacts, in: Papale, P. (Ed.), *Forecasting and Planning for Volcanic*  
854 *Hazards, Risks, and Disasters*. Elsevier, pp. 473–491. [https://doi.org/10.1016/B978-0-  
855 \*12-818082-2.00012-3\*](https://doi.org/10.1016/B978-0-12-818082-2.00012-3)
- 856 Blake, D., Wilson, G., Stewart, C., Craig, H., Hayes, J.L., Jenkins, S.F., Wilson, T., Horwell,  
857 C.J., Andreastuti, S., Daniswara, R., Ferdijwijaya, S., Leonard, G., Hendrasto, M.,  
858 Cronin, S.J., 2015. The 2014 eruption of Kelud volcano, Indonesia: impacts on  
859 infrastructure, utilities, agriculture and health. *GNS Science Report 2015/15*, GNS  
860 Science, Te Pu Ao.
- 861 Bonadonna, C., Cioni, R., Pistolesi, M., Elissondo, M., Baumann, V., 2015. Sedimentation of  
862 long-lasting wind-affected volcanic plumes: the example of the 2011 rhyolitic Cordón  
863 Caulle eruption, Chile. *Bull. Volcanol.* 77, 1–19. [https://doi.org/10.1007/s00445-015-  
864 \*0900-8\*](https://doi.org/10.1007/s00445-015-0900-8)
- 865 Bright, B.C., Hudak, A.T., Kennedy, R.E., Braaten, J.D., Henareh Khalyani, A., 2019.  
866 Examining post-fire vegetation recovery with Landsat time series analysis in three  
867 western North American forest types. *Fire Ecol.* 15. [https://doi.org/10.1186/s42408-  
868 \*018-0021-9\*](https://doi.org/10.1186/s42408-018-0021-9)
- 869 Buchhorn, M., Smets, B., Bertels, L., Roo, B.D., Lesiv, M., Tsendbazar, N.-E., Herold, M.,  
870 Fritz, S., 2020. Copernicus Global Land Service: Land Cover 100m: collection 3: epoch  
871 2018: Globe. <https://doi.org/10.5281/ZENODO.3518038>
- 872 Cai, Z., Jönsson, P., Jin, H., Eklundh, L., 2017. Performance of smoothing methods for  
873 reconstructing NDVI time-series and estimating vegetation phenology from MODIS  
874 data. *Remote Sens.* 9, 20–22. <https://doi.org/10.3390/rs9121271>
- 875 Campos-Taberner, M., Moreno-Martínez, Á., García-Haro, F.J., Camps-Valls, G., Robinson,  
876 N.P., Kattge, J., Running, S.W., 2018. Global estimation of biophysical variables from  
877 Google Earth Engine platform. *Remote Sens.* 10, 1–17.  
878 <https://doi.org/10.3390/rs10081167>
- 879 Chen, T., Guestrin, C., 2016. XGBoost: A Scalable Tree Boosting System. *Proc. 22nd ACM*  
880 *SIGKDD Int. Conf. Knowl. Discov. Data Min.* 785–794.  
881 <https://doi.org/10.1145/2939672.2939785>
- 882 Chou, W., Lin, W., Lin, C., 2009. Vegetation recovery patterns assessment at landslides caused  
883 by catastrophic earthquake: A case study in central Taiwan. *Env. Monit Assess* 152.  
884 <https://doi.org/10.1007/s10661-008-0312-8>
- 885 Choumert, J., Phinélias, P., 2018. Volcanic hazards , land and labor, *Etudes et Documents*.  
886 CERDI, Pole Tertiaire, Clermont Ferrand.



- 887 Collini, E., Osores, M.S., Folch, A., Viramonte, J.G., Villarosa, G., Salmuni, G., 2013. Volcanic  
888 ash forecast during the June 2011 Cordón Caulle eruption. *Nat. Hazards* 66, 389–412.  
889 <https://doi.org/10.1007/s11069-012-0492-y>
- 890 Costa, A., Pioli, L., Bonadonna, C., 2016. Assessing tephra total grain-size distribution: Insights  
891 from field data analysis. *Earth Planet. Sci. Lett.* 443, 90–107.  
892 <https://doi.org/10.1016/j.epsl.2016.02.040>
- 893 Craig, H., Wilson, T., Stewart, C., Outes, V., Villarosa, G., Baxter, P., 2016a. Impacts to  
894 agriculture and critical infrastructure in Argentina after ashfall from the 2011 eruption  
895 of the Cordón Caulle volcanic complex: an assessment of published damage and  
896 function thresholds. *J. Appl. Volcanol.* 5, 7. [https://doi.org/10.1186/s13617-016-0046-](https://doi.org/10.1186/s13617-016-0046-1)  
897 1
- 898 Craig, H.M., Wilson, T.M., Magill, C., Stewart, C., Wild, A.J., 2021. Agriculture and forestry  
899 impact assessment for tephra fall hazard: fragility function development and New  
900 Zealand scenario application. *Volcanica* 4, 345–367.  
901 <https://doi.org/10.30909/vol.04.02.345367>
- 902 Crisafulli, C., Swanson, F., Halvorson, J., Clarkson, B., 2015. Volcano Ecology: Disturbance  
903 Characteristics and Assembly of Biological Communities, in: Sigurdsson, H.,  
904 Houghton, B., McNutt, S., Rymer, H., Stix, J. (Eds.), *The Encyclopedia of Volcanoes*,  
905 2nd Edition. Academic Press, San Diego, pp. 1265–1284.
- 906 Cronin, S.J., Stewart, C., Zernack, A.V., Brenna, M., Procter, J.N., Pardo, N., Christenson, B.,  
907 Wilson, T., Stewart, R.B., Irwin, M., 2014. Volcanic ash leachate compositions and  
908 assessment of health and agricultural hazards from 2012 hydrothermal eruptions,  
909 Tongariro, New Zealand. *J. Volcanol. Geotherm. Res.*  
910 <https://doi.org/10.1016/j.jvolgeores.2014.07.002>
- 911 Crowley, M.A., Cardille, J.A., White, J.C., Wulder, M.A., 2019. Generating intra-year metrics  
912 of wildfire progression using multiple open-access satellite data streams. *Remote Sens.*  
913 *Environ.* 232, 111295. <https://doi.org/10.1016/j.rse.2019.111295>
- 914 Dale, V., Swanson, F.J., Crisafulli, C.M., 2005. Ecological Responses to the 1980 Eruption of  
915 Mount St. Helens.
- 916 de Rose, R.C., Ogushi, T., Morishima, W., Collado, M., 2011. Land cover change on Mt.  
917 Pinatubo, the Philippines, monitored using ASTER VNIR. *Int J Remote Sens.* 32, 9279–  
918 9305. <https://doi.org/10.1080/01431161.2011.554452>
- 919 De Schutter, A., Kervyn, M., Canters, F., Bosshard-Stadlin, S.A., Songo, M.A.M., Mattsson,  
920 H.B., 2015. Ash fall impact on vegetation: a remote sensing approach of the Oldoinyo  
921 Lengai 2007–08 eruption. *J. Appl. Volcanol.* 4, 15. [https://doi.org/10.1186/s13617-015-](https://doi.org/10.1186/s13617-015-0032-z)  
922 0032-z
- 923 Degruyter, W., Bonadonna, C., 2012. Improving on mass flow rate estimates of volcanic  
924 eruptions. *Geophys Res Lett* 39. <https://doi.org/10.1029/2012GL052566>



- 925 Delmelle, P., Opfergelt, S., Cornelis, J., Chien-Lu, P., 2015. Volcanic Soils, in: Sigurdsson, H.,  
926 Houghton, B., McNutt, S., Rymer, H., Stix, J. (Eds.), *The Encyclopedia of Volcanoes*,  
927 2nd Edition. Academic Press, SanDiego, pp. 1253–1264.
- 928 DeVries, B., Huang, C., Armston, J., Huang, W., Jones, J.W., Lang, M.W., 2020. Rapid and  
929 robust monitoring of flood events using Sentinel-1 and Landsat data on the Google Earth  
930 Engine. *Remote Sens. Environ.* 240, 111664. <https://doi.org/10.1016/j.rse.2020.111664>
- 931 Dominguez, L., Bonadonna, C., Forte, P., Jarvis, P.A., Cioni, R., Mingari, L., Bran, D.,  
932 Panebianco, J.E., 2020a. Aeolian Remobilisation of the 2011-Cordón Caulle Tephra-  
933 Fallout Deposit: Example of an Important Process in the Life Cycle of Volcanic Ash.  
934 *Front. Earth Sci.* 7, 1–20. <https://doi.org/10.3389/feart.2019.00343>
- 935 Dominguez, L., Rossi, E., Mingari, L., Bonadonna, C., Forte, P., Panebianco, J.E., Bran, D.,  
936 2020b. Mass flux decay timescales of volcanic particles due to aeolian processes in the  
937 Argentinian Patagonia steppe. *Sci. Rep.* 10, 1–15. <https://doi.org/10.1038/s41598-020-71022-w>
- 939 Easdale, M.H., Bruzzone, O., 2018. Spatial distribution of volcanic ash deposits of 2011  
940 Puyehue-Cordón Caulle eruption in Patagonia as measured by a perturbation in NDVI  
941 temporal dynamics. *J. Volcanol. Geotherm. Res.* 353, 11–17.  
942 <https://doi.org/10.1016/j.jvolgeores.2018.01.020>
- 943 Elissondo, M., Baumann, V., Bonadonna, C., Pistolesi, M., Cioni, R., Bertagnini, A., Biass, S.,  
944 Herrero, J.-C., Gonzalez, R., 2016. Chronology and impact of the 2011 Cordón Caulle  
945 eruption, Chile. *Nat Hazards Earth Syst Sci* 16, 675–704. <https://doi.org/10.5194/nhess-16-675-2016>
- 947 Enriquez, A.S., Nepalova, M., Cremona, M.V., Peri, P.L., Six, J., 2021. Immobilization and  
948 stabilization of volcanic ash in soil aggregates in semiarid meadows of Northern  
949 Patagonia. *Geoderma* 392, 114987. <https://doi.org/10.1016/j.geoderma.2021.114987>
- 950 FAO, 2018. *The Impact of disasters and crises on agriculture and Food Security*. Food and  
951 Agriculture Organisation, Rome.
- 952 Farr, T.G., Rosen, P.A., Caro, E., Crippen, R., Duren, R., Hensley, S., Kobrick, M., Paller, M.,  
953 Rodriguez, E., Roth, L., Seal, D., Shaffer, S., Shimada, J., Umland, J., Werner, M.,  
954 Oskin, M., Burbank, D., Alsdorf, D., 2007. The Shuttle Radar Topography Mission.  
955 *Rev. Geophys.* 45, RG2004. <https://doi.org/10.1029/2005RG000183>
- 956 Few, R., Armijos, M.T., Barclay, J., 2017. Living with Volcan Tungurahua: The dynamics of  
957 vulnerability during prolonged volcanic activity. *Geoforum* 80, 72–81.  
958 <https://doi.org/10.1016/j.geoforum.2017.01.006>
- 959 Folch, A., Costa, A., Macedonio, G., 2016. FPLUME-1.0: An integral volcanic plume model  
960 accounting for ash aggregation. *Geosci Model Dev* 9, 431–450.  
961 <https://doi.org/10.5194/gmd-9-431-2016>
- 962 Folch, A., Mingari, L., Gutierrez, N., Hanzich, M., Macedonio, G., Costa, A., Prata, A.,  
963 Mingari, L., Folch, A., Macedonio, G., Costa, A., 2021. FALL3D-8.0: A computational  
964 model for atmospheric transport and deposition of particles, aerosols and radionuclides



- 965 - Part 2: Model validation. *Geosci. Model Dev.* 14, 409–436.  
966 <https://doi.org/10.5194/gmd-13-1431-2020>
- 967 Folch, A., Mingari, L., Osores, M.S., Collini, E., 2014. Modeling volcanic ash resuspension –  
968 application to the 14–18 October 2011 outbreak episode in central Patagonia, Argentina.  
969 *Nat Hazards Earth Syst Sci* 14, 119–133. <https://doi.org/10.5194/nhess-14-119-2014>
- 970 Forte, P., Domínguez, L., Bonadonna, C., Gregg, C.E., Bran, D., Bird, D., Castro, J.M., 2017.  
971 Ash resuspension related to the 2011–2012 Cordón Caulle eruption, Chile, in a rural  
972 community of Patagonia, Argentina. *J. Volcanol. Geotherm. Res.*  
973 <https://doi.org/10.1016/j.jvolgeores.2017.11.021>
- 974 Freire, S., Florczyk, A., Pesaresi, M., Sliuzas, R., 2019. An Improved Global Analysis of  
975 Population Distribution in Proximity to Active Volcanoes, 1975–2015. *ISPRS Int. J.*  
976 *Geo-Inf.* 8, 341. <https://doi.org/10.3390/ijgi8080341>
- 977 Giuliani, G., Camara, G., Killough, B., Minchin, S., 2019. Earth observation open science:  
978 enhancing reproducible science using data cubes. *Data* 4, 4–9.  
979 <https://doi.org/10.3390/data4040147>
- 980 Gomes, V.C.F., Queiroz, G.R., Ferreira, K.R., 2020. An overview of platforms for big earth  
981 observation data management and analysis. *Remote Sens.* 12, 1–25.  
982 <https://doi.org/10.3390/RS12081253>
- 983 Gonzalez-Roglich, M., Zvoleff, A., Noon, M., Liniger, H., Fleiner, R., Harari, N., Garcia, C.,  
984 2019. Synergizing global tools to monitor progress towards land degradation neutrality:  
985 Trends.Earth and the World Overview of Conservation Approaches and Technologies  
986 sustainable land management database. *Environ. Sci. Policy* 93, 34–42.  
987 <https://doi.org/10.1016/j.envsci.2018.12.019>
- 988 Gorelick, N., Hancher, M., Dixon, M., Ilyushchenko, S., Thau, D., Moore, R., 2017. Google  
989 Earth Engine: Planetary-scale geospatial analysis for everyone. *Remote Sens. Environ.*  
990 202, 18–27. <https://doi.org/10.1016/j.rse.2017.06.031>
- 991 He, W., Ye, C., Sun, J., Xiong, J., Wang, J., Zhou, T., 2020. Dynamics and drivers of the alpine  
992 timberline on Gongga Mountain of Tibetan Plateau-Adopted from the Otsu method on  
993 Google Earth engine. *Remote Sens.* 12, 1–20. <https://doi.org/10.3390/RS12162651>
- 994 Hengl, T., De Jesus, J.M., Heuvelink, G.B.M., Gonzalez, M.R., Kilibarda, M., Blagotić, A.,  
995 Shangguan, W., Wright, M.N., Geng, X., Bauer-Marschallinger, B., Guevara, M.A.,  
996 Vargas, R., MacMillan, R.A., Batjes, N.H., Leenaars, J.G.B., Ribeiro, E., Wheeler, I.,  
997 Mantel, S., Kempen, B., 2017. SoilGrids250m: Global gridded soil information based  
998 on machine learning, *PLoS ONE*. <https://doi.org/10.1371/journal.pone.0169748>
- 999 Hersbach, H., Bell, B., Berrisford, P., Hirahara, S., Horányi, A., Muñoz-Sabater, J., Nicolas, J.,  
1000 Peubey, C., Radu, R., Schepers, D., Simmons, A., Soci, C., Abdalla, S., Abellan, X.,  
1001 Balsamo, G., Bechtold, P., Biavati, G., Bidlot, J., Bonavita, M., De Chiara, G.,  
1002 Dahlgren, P., Dee, D., Diamantakis, M., Dragani, R., Flemming, J., Forbes, R., Fuentes,  
1003 M., Geer, A., Haimberger, L., Healy, S., Hogan, R.J., Hólm, E., Janisková, M., Keeley,  
1004 S., Laloyaux, P., Lopez, P., Lupu, C., Radnoti, G., de Rosnay, P., Rozum, I., Vamborg,



- 1005 F., Villaume, S., Thépaut, J.N., 2020. The ERA5 global reanalysis. Q. J. R. Meteorol.  
1006 Soc. 146, 1999–2049. <https://doi.org/10.1002/qj.3803>
- 1007 Hope, A., Albers, N., Bart, R., 2012. Characterizing post-fire recovery of fynbos vegetation in  
1008 the western cape region of south africa using MODIS data. Int J Remote Sens. 33.  
1009 <https://doi.org/10.1080/01431161.2010.543184>
- 1010 Hotes, S., Poschlod, P., Takahashi, H., Grootjans, A.P., Adema, E., 2004. Effects of tephra  
1011 deposition on mire vegetation: a field experiment in Hokkaido, Japan: *Tephra effects on*  
1012 *mire vegetation*. J. Ecol. 92, 624–634. [https://doi.org/10.1111/j.0022-](https://doi.org/10.1111/j.0022-0477.2004.00901.x)  
1013 [0477.2004.00901.x](https://doi.org/10.1111/j.0022-0477.2004.00901.x)
- 1014 Huete, A.R., Didana, K., Miuraa, T., Rodriguez, E.P., Gao, X., Ferreira, L.G., 2002.  
1015 Overview of the radiometric and biophysical performance of the MODIS vegetation  
1016 indices. Remote Sens. Environ. 83. [https://doi.org/10.1016/S0034-4257\(02\)00096-2](https://doi.org/10.1016/S0034-4257(02)00096-2)
- 1017 Jenkins, S.F., Wilson, T.M., Magill, C., Miller, V., Stewart, C., 2014. Volcanic ash fall hazard  
1018 and risk: Technical Background Paper for the UN-ISDR 2015 Global Assessment  
1019 Report on Disaster Risk Reduction, Mln. Global Volcano Model and IAVCEI.
- 1020 Jenkins, S.F., Wilson, T.M., Magill, C., Miller, V., Stewart, C., Blong, R., Marzocchi, W.,  
1021 Boulton, M., Bonadonna, C., Costa, A., 2015. Volcanic ash fall hazard and risk, in:  
1022 Loughlin, S., Sparks, S., Brown, S., Jenkins, S., Vye-Brown, C. (Eds.), Global Volcanic  
1023 Hazards and Risk. Cambridge University Press, pp. 173–222.
- 1024 Jin, Z., Azzari, G., You, C., Di Tommaso, S., Aston, S., Burke, M., Lobell, D.B., 2019.  
1025 Smallholder maize area and yield mapping at national scales with Google Earth Engine.  
1026 Remote Sens. Environ. 228, 115–128. <https://doi.org/10.1016/j.rse.2019.04.016>
- 1027 Kalisa, W., Igbawua, T., Henchiri, M., Ali, S., Zhang, S., Bai, Y., Zhang, J., 2019. Assessment  
1028 of climate impact on vegetation dynamics over East Africa from 1982 to 2015. Sci. Rep.  
1029 9, 1–20. <https://doi.org/10.1038/s41598-019-53150-0>
- 1030 Khanal, N., Matin, M.A., Uddin, K., Poortinga, A., Chishtie, F., Tenneson, K., Saah, D., 2020.  
1031 A comparison of three temporal smoothing algorithms to improve land cover  
1032 classification: A case study from NEPAL. Remote Sens. 12, 5–7.  
1033 <https://doi.org/10.3390/RS12182888>
- 1034 Kong, D., Zhang, Y., Gu, X., Wang, D., 2019. A robust method for reconstructing global  
1035 MODIS EVI time series on the Google Earth Engine. ISPRS J. Photogramm. Remote  
1036 Sens. 155, 13–24. <https://doi.org/10.1016/j.isprsjprs.2019.06.014>
- 1037 Le Pennec, J.-L., Ruiz, G.A., Ramón, P., Palacios, E., Mothes, P., Yepes, H., 2012. Impact of  
1038 tephra falls on Andean communities: The influences of eruption size and weather  
1039 conditions during the 1999–2001 activity of Tungurahua volcano, Ecuador. J. Volcanol.  
1040 Geotherm. Res. 217–218, 91–103. <https://doi.org/10.1016/j.jvolgeores.2011.06.011>
- 1041 Leadbetter, S.J., Hort, M.C., von Löwis, S., Weber, K., Witham, C.S., 2012. Modeling the  
1042 resuspension of ash deposited during the eruption of Eyjafjallajökull in spring 2010:  
1043 MODELING RESUSPENDED VOLCANIC ASH. J. Geophys. Res. Atmospheres 117.  
1044 <https://doi.org/10.1029/2011JD016802>



- 1045 Lebon, S.L.G., 2009. Volcanic activity and environment: Impacts on agriculture and use of  
1046 geological data to improve recovery processes.
- 1047 Lehmann, A., Nativi, S., Mazzetti, P., Maso, J., Serral, I., 2020. GEOEssential – mainstreaming  
1048 work flows from data sources to environment policy indicators with essential variables  
1049 13, 322–338.
- 1050 Li, L., Bakelants, L., Solana, C., Canters, F., Kervyn, M., 2018. Dating lava flows of tropical  
1051 volcanoes by means of spatial modeling of vegetation recovery. *Earth Surf. Process.*  
1052 *Landf.* 43, 840–856. <https://doi.org/10.1002/esp.4284>
- 1053 Lin, Y.C., Mestav Sarica, G., Chua, T.J., Jenkins, S.F., Switzer, A.D., Woo, G., Lallemand, D.,  
1054 2021. Asia’s looming Black Elephant events. *Commun. Earth Environ.* 2, 214.  
1055 <https://doi.org/10.1038/s43247-021-00283-8>
- 1056 Liu, E.J., Cashman, K.V., Beckett, F.M., Witham, C.S., Leadbetter, S.J., Hort, M.C.,  
1057 Guðmundsson, S., 2014. Ash mists and brown snow: Remobilization of volcanic ash  
1058 from recent Icelandic eruptions. *J. Geophys. Res. Atmospheres* 119, 2014JD021598.  
1059 <https://doi.org/10.1002/2014JD021598>
- 1060 Liu, L., Xiao, X., Qin, Y., Wang, J., Xu, X., Hu, Y., Qiao, Z., 2020a. Mapping cropping  
1061 intensity in China using time series Landsat and Sentinel-2 images and Google Earth  
1062 Engine. *Remote Sens. Environ.* 239, 111624. <https://doi.org/10.1016/j.rse.2019.111624>
- 1063 Lu, T., Zeng, H., Luo, Y., Wang, Q., Shi, F., Sun, G., Wu, Y., Wu, N., 2012. Monitoring  
1064 vegetation recovery after China’s May 2008 wenchuan earthquake using landsat TM  
1065 time-series data: a case study in Mao county. *Ecol Res* 27.  
1066 <https://doi.org/10.1007/s11284-012-0976-y>
- 1067 Lundberg, S.M., Erion, G., Chen, H., DeGrave, A., Prutkin, J.M., Nair, B., Katz, R.,  
1068 Himmelfarb, J., Bansal, N., Lee, S.-I., 2020. From local explanations to global  
1069 understanding with explainable AI for trees. *Nat. Mach. Intell.* 2, 56–67.  
1070 <https://doi.org/10.1038/s42256-019-0138-9>
- 1071 Magill, C., Wilson, T., Okada, T., 2013. Observations of tephra fall impacts from the 2011  
1072 Shinmoedake eruption, Japan. *Earth Planets Space* 65, 677–698.  
1073 <https://doi.org/10.5047/eps.2013.05.010>
- 1074 Mahecha, M.D., Gans, F., Brandt, G., Christiansen, R., Cornell, S.E., Fomferra, N., Kraemer,  
1075 G., Peters, J., Bodesheim, P., Camps-Valls, G., F. Donges, J., Dorigo, W., M. Estupinan-  
1076 Suarez, L., H. Gutierrez-Velez, V., Gutwin, M., Jung, M., C. Londoño, M., G. Miralles,  
1077 D., Papastefanou, P., Reichstein, M., 2020. Earth system data cubes unravel global  
1078 multivariate dynamics. *Earth Syst. Dyn.* 11, 201–234. [https://doi.org/10.5194/esd-11-  
1079 201-2020](https://doi.org/10.5194/esd-11-201-2020)
- 1080 Major, J.J., Bertin, D., Pierson, T.C., Amigo, Á., Iroumé, A., Ulloa, H., Castro, J., 2016.  
1081 Extraordinary sediment delivery and rapid geomorphic response following the 2008-  
1082 2009 eruption of Chaitén Volcano, Chile. *Water Resour. Res.* 52, 5075–5094.  
1083 <https://doi.org/10.1002/2015WR018250>



- 1084 Martín-Sotoca, J.J., Saa-Requejo, A., Moratiel, R., Dalezios, N., Faraslís, I., María Tarquis, A.,  
1085 2019. Statistical analysis for satellite-index-based insurance to define damaged pasture  
1086 thresholds. *Nat. Hazards Earth Syst. Sci.* 19, 1685–1702. [https://doi.org/10.5194/nhess-](https://doi.org/10.5194/nhess-19-1685-2019)  
1087 19-1685-2019
- 1088 Marzen, L., Szantoib, Z., Harrington, L.M.B., Harrington, J.A., 2011. Implications of  
1089 management strategies and vegetation change in the Mount St. Helens blast zone.  
1090 *Geocarto Int.* 26. <https://doi.org/10.1080/10106049.2011.584977>
- 1091 Meroni, M., Fasbender, D., Rembold, F., Atzberger, C., Klisch, A., 2019. Near real-time  
1092 vegetation anomaly detection with MODIS NDVI: Timeliness vs. accuracy and effect  
1093 of anomaly computation options. *Remote Sens. Environ.* 221, 508–521.  
1094 <https://doi.org/10.1016/j.rse.2018.11.041>
- 1095 Molnar, C., 2021. *Interpretable Machine Learning*.
- 1096 Müller, A.C., Guido, S., 2015. *Introduction to Machine Learning with Python and Scikit-Learn*,  
1097 O'Reilly Media, Inc.
- 1098 Murphy, S., Wright, R., Rouwet, D., 2017. Color and temperature of the crater lakes at  
1099 Kelimutu volcano through time. *Bull. Volcanol.* 80, 2. [https://doi.org/10.1007/s00445-](https://doi.org/10.1007/s00445-017-1172-2)  
1100 017-1172-2
- 1101 Nativi, S., Santoro, M., Giuliani, G., Mazzetti, P., 2020. Towards a knowledge base to support  
1102 global change policy goals. *Int. J. Digit. Earth* 13, 188–216.  
1103 <https://doi.org/10.1080/17538947.2018.1559367>
- 1104 Osman, S., Rossi, E., Bonadonna, C., Frischknecht, C., Andronico, D., Cioni, R., Scollo, S.,  
1105 2019. Exposure-based risk assessment and emergency management associated with the  
1106 fallout of large clasts at Mount Etna. *Nat. Hazards Earth Syst. Sci.* 19, 589–610.  
1107 <https://doi.org/10.5194/nhess-19-589-2019>
- 1108 Pfeiffer, T., Costa, A., Macedonio, G., 2005. A model for the numerical simulation of tephra  
1109 fall deposits. *J. Volcanol. Geotherm. Res.* 140, 273–294.  
1110 <https://doi.org/10.1016/j.jvolgeores.2004.09.001>
- 1111 Phillips, J., Barclay, J., Pyle, D., Armijos, M.T., 2019. Dynamic and Extensive Risk Arising  
1112 from Volcanic Ash Impacts on Agriculture, in: *Global Assessment Report on Disaster  
1113 Risk Reduction (GAR 2019)*. United Nations Office for Disaster Risk Reduction, pp.  
1114 1–30.
- 1115 Pierson, Thomas C., Major, Jon J., Amigo, Á., Moreno, H., 2013. Acute sedimentation response  
1116 to rainfall following the explosive phase of the 2008–2009 eruption of Chaitén volcano,  
1117 Chile. *Bull. Volcanol.* 75, 1–17. <https://doi.org/10.1007/s00445-013-0723-4>
- 1118 Pistolesi, M., Cioni, R., Bonadonna, C., Elissondo, M., Baumann, V., Bertagnini, A., Chiari,  
1119 L., Gonzales, R., Rosi, M., Francalanci, L., 2015. Complex dynamics of small-moderate  
1120 volcanic events: the example of the 2011 rhyolitic Cordón Caulle eruption, Chile. *Bull.*  
1121 *Volcanol.* 77, 1–24. <https://doi.org/10.1007/s00445-014-0898-3>



- 1122 Poortinga, A., Clinton, N., Saah, D., Cutter, P., Chishtie, F., Markert, K.N., Anderson, E.R.,  
1123 Troy, A., Fenn, M., Tran, L.H., Bean, B., Nguyen, Q., Bhandari, B., Johnson, G.,  
1124 Towashiraporn, P., 2018. An operational before-after-control-impact (BACI) designed  
1125 platform for vegetation monitoring at planetary scale. *Remote Sens.* 10.  
1126 <https://doi.org/10.3390/rs10050760>
- 1127 Poulidis, A.P., Biass, S., Bagheri, G., Takemi, T., Iguchi, M., 2021. Atmospheric vertical  
1128 velocity - a crucial component in understanding proximal deposition of volcanic ash.  
1129 *Earth Planet. Sci. Lett.* 566, 116980. <https://doi.org/10.1016/j.epsl.2021.116980>
- 1130 Rampengan, M.M.F., Boedhihartono, A.K., Margules, C., Sayer, J., Law, L., Gaillard, J.C.,  
1131 Tien, O.T.N., Linh, T.T.M., 2016. Agroforestry on an Active Volcanic Small Island in  
1132 Indonesia: Prospering with Adversity. *Geogr. Res.* 54, 19–34.  
1133 <https://doi.org/10.1111/1745-5871.12148>
- 1134 ReliefWeb, 2020. Philippines: Taal Volcano - Jan 2020.
- 1135 Rembold, F., Meroni, M., Urbano, F., Csak, G., Kerdiles, H., Perez-Hoyos, A., Lemoine, G.,  
1136 Leo, O., Negre, T., 2019. ASAP: A new global early warning system to detect anomaly  
1137 hot spots of agricultural production for food security analysis. *Agric. Syst.* 168, 247–  
1138 257. <https://doi.org/10.1016/j.agry.2018.07.002>
- 1139 Rowley, J., 2007. The wisdom hierarchy: Representations of the DIKW hierarchy. *J. Inf. Sci.*  
1140 33, 163–180. <https://doi.org/10.1177/0165551506070706>
- 1141 Runge, J., Bathiany, S., Boltt, E., Camps-Valls, G., Coumou, D., Deyle, E., Glymour, C.,  
1142 Kretschmer, M., Mahecha, M.D., Muñoz-Marí, J., van Nes, E.H., Peters, J., Quax, R.,  
1143 Reichstein, M., Scheffer, M., Schölkopf, B., Spirtes, P., Sugihara, G., Sun, J., Zhang,  
1144 K., Zscheischler, J., 2019. Inferring causation from time series in Earth system sciences.  
1145 *Nat. Commun.* 10, 2553. <https://doi.org/10.1038/s41467-019-10105-3>
- 1146 Shapley, L.S., 1956. A Value for n-Person Games, in: Kuhn, H.W., Tucker, A.W. (Eds.),  
1147 *Contributions to the Theory of Games* 2.28. Princeton University Press, pp. 307–318.  
1148 <https://doi.org/doi:10.1515/9781400881970-018>
- 1149 Sivarajan, S.P., Lindsay, J., Cronin, S., Wilson, T., 2017. Remediation and Recovery  
1150 Techniques for Volcanic Ash-Affected Pasture Soils of New Zealand, in: Currie, L.D.,  
1151 Hedley, M.J. (Eds.), *Science and Policy: Nutrient Management Challenges for the next*  
1152 *Generation. Fertilizer and Lime Research Centre, Massey University, Palmerston North,*  
1153 *New Zealand, Massey*, pp. 1–17.
- 1154 Skamarock, W.C., Klemp, J.B., Dudhia, J., Gill, D.O., Liu, Z., Berner, J., Wang, W., Powers,  
1155 J.G., Duda, M.G., Barker, D., Huang, X., 2019. A Description of the Advanced  
1156 Research WRF Model Version 4. NCAR. <https://doi.org/10.5065/1dfh-6p97>
- 1157 Stewart, C., Craig, H.M., Gaw, S., Wilson, T., Villarosa, G., Outes, V., Cronin, S., Oze, C.,  
1158 2016. Fate and agricultural consequences of leachable elements added to the  
1159 environment from the 2011 Cordon Caulle tephra fall. *J. Volcanol. Geotherm. Res.* 327,  
1160 554–570. <https://doi.org/10.1016/j.jvolgeores.2016.09.017>





- 1161 Stewart, C., Damby, D.E., Tomašek, I., Horwell, C.J., Plumlee, G.S., Armienta, M.A.,  
1162 Hinojosa, M.G.R., Appleby, M., Delmelle, P., Cronin, S., Ottley, C.J., Oppenheimer,  
1163 C., Morman, S., 2020. Assessment of leachable elements in volcanic ashfall: a review  
1164 and evaluation of a standardized protocol for ash hazard characterization. *J. Volcanol.*  
1165 *Geotherm. Res.* 392. <https://doi.org/10.1016/j.jvolgeores.2019.106756>
- 1166 Sulova, A., Arsanjani, J.J., 2021. Exploratory Analysis of Driving Force of Wildfires in  
1167 Australia : An Application of Machine Learning within Google Earth Engine. *Remote*  
1168 *Sens.* 13, 23. <https://dx.doi.org/10.3390/rs13010010>
- 1169 Tamiminia, H., Salehi, B., Mahdianpari, M., Quackenbush, L., Adeli, S., Brisco, B., 2020.  
1170 Google Earth Engine for geo-big data applications: A meta-analysis and systematic  
1171 review. *ISPRS J. Photogramm. Remote Sens.* 164, 152–170.  
1172 <https://doi.org/10.1016/j.isprsjprs.2020.04.001>
- 1173 The World Bank, 2018. Evaluación de daños y pérdidas del Volcán de Fuego (No.  
1174 AUS0000800).
- 1175 Tortini, R., van Manen, S.M., Parkes, B.R.B., Carn, S.A., 2017. The impact of persistent  
1176 volcanic degassing on vegetation: A case study at Turrialba volcano, Costa Rica. *Int. J.*  
1177 *Appl. Earth Obs. Geoinformation* 59, 92–103. <https://doi.org/10.1016/j.jag.2017.03.002>
- 1178 Wang, L., Diao, C., Xian, G., Yin, D., Lu, Y., Zou, S., Erickson, T.A., 2020. A summary of the  
1179 special issue on remote sensing of land change science with Google earth engine.  
1180 *Remote Sens. Environ.* 248. <https://doi.org/10.1016/j.rse.2020.112002>
- 1181 Wilson, T., Cole, J., Cronin, S., Stewart, C., 2011. Impacts on agriculture following the 1991  
1182 eruption of Vulcan Hudson, Patagonia: lessons for recovery. *Nat. Hazards* 57, 185–212.
- 1183 Wilson, T., Cole, J., Stewart, C., Cronin, S., Johnston, D., 2011. Ash storms: impacts of wind-  
1184 remobilised volcanic ash on rural communities and agriculture following the 1991  
1185 Hudson eruption, southern Patagonia, Chile. *Bull. Volcanol.* 73, 223–239.
- 1186 Wilson, T., Kaye, G., Stewart, C., Cole, J., 2007. Impacts of the 2006 eruption of Merapi  
1187 volcano, Indonesia, on agriculture and infrastructure, GNS Science Report 2007/07.
- 1188 Wilson, T., Stewart, C., Bickerton, H., Baxter, P., Outes, V., Villarosa, G., E, R., 2013. Impacts  
1189 of the June 2011 Puyehue-Cordón Caulle volcanic complex eruption on urban  
1190 infrastructure, agriculture and public health. GNS Science Report 2012/20.
- 1191 Zhang, Y., Kong, D., Gan, R., Chiew, F.H.S., McVicar, T.R., Zhang, Q., Yang, Y., 2019.  
1192 Coupled estimation of 500 m and 8-day resolution global evapotranspiration and gross  
1193 primary production in 2002–2017. *Remote Sens. Environ.* 222, 165–182.  
1194 <https://doi.org/10.1016/j.rse.2018.12.031>
- 1195



	Code: DS0	DS1	DS2	DS3	DS4	DS5
<b>Description</b>	<b>No damage</b>	<b>Disruption to harvest operations and livestock grazing of exposed feed</b>	<b>Minor productivity loss: less than 50 %/crop</b>	<b>Major productivity loss: more than 50 %/crop; Remediation required</b>	<b>Total crop loss; Substantial remediation required</b>	<b>Major rehabilitation required/ Retirement of land</b>
<b>Agriculture type</b>						
<b>Horticultural/Arable</b>	0 mm (0-20 mm)	1 mm (0.1-50 mm)	5 mm (1-50 mm)	50 mm (1-100 mm)	100 mm (25-200 mm)	250 mm (100-400 mm)
<b>Pastoral</b>	0 mm (0-20 mm)	1 mm (0.1-50 mm)	25 mm (1-70 mm)	60 mm (20-150 mm)	100 mm (30-200 mm)	250 mm (100-400 mm)
<b>Paddies</b>	0 mm (0-50 mm)	3 mm (0.1-50 mm)	30 mm (1-75 mm)	75 mm (20-300 mm)	150 (75-300 mm)	250 mm (100-500 mm)
<b>Forestry</b>	0 mm (0-75 mm)	5 mm (0.1-75 mm)	200 mm (20-300 mm)	1000 mm (100-2000 mm)	1500 mm (100-2000 mm)	N/A

**Table 1 :** Damage/disruption states (DS1–5) as a function of the dry deposit thickness as hazard proxy identified by Jenkins et al., (2014) based on literature review. DDS assume that crops are in the growing stage. Hazard metrics include the median and interdecile deposit thicknesses inferred from expert judgement and empirical data.



Data provider	Variable	Description	Resolution
<b>MODIS</b>	minV	Target variable for magnitude of impact	250 m
	mint	Target variable for timing of impact	
	EVI	Mean EVI value averaged over 1 year of pre-eruption data	
<b>Fall3D</b>	EVI_stdDev	Standard deviation of EVI value averaged over 1 year of pre-eruption data	
	lapilli	Lapilli mass load (kg/m <sup>2</sup> )	0.033 deg.
	coarse_ash	Coarse ash mass load (kg/m <sup>2</sup> )	
<b>SRTM</b>	fine_ash	Fine ash mass load (kg/m <sup>2</sup> )	
	elevation	Terrain elevation (m asl)	90 m
	slope	Terrain slope (degrees)	
<b>ERAS</b>	aspect	Terrain aspect (degrees)	
	northness	Cosine of aspect	
	eastness	Sine of aspect	
	total_precipitation_n	Total precipitation (m)	
	total_precipitation_SRI_n	Anomaly in total precipitation	0.1 deg.
<b>Copernicus</b>	temperature_2m_n	Air temperature (°K) at a 2 m elevation	
	temperature_2m_SRI_n	Anomaly in air temperature	
	wind_10	Wind speed (m/s) at a 10 m elevation	
<b>Other</b>	landcover	Copernicus global land cover layer	100 m
	climate	Köppen climate classification	1000 m
	soil	Soilgrid	250 m

Note: The total\_precipitation and temperature\_2m variables are calculated for  $n=1, 2, 3, 6$  and 12 months

**Table 2** : Summary of variables used in the model.



Run	Plume model	Plume param.	TGSD
a	Top Hat	Thickness = 2000 m	Bi-Weibull
b	Suzuki	A=4, L=5	Bi-Weibull
c	Top Hat	Thickness = 2000 m	Gaussian
d	Suzuki	A=4, L=5	Gaussian
e	Fplume	Solved for MFR	Bi-Weibull
f	Fplume	Solved for MFR	Gaussian

**Table 3** : Initial parameters to the Fall3d runs. For the Suzuki plume model,  $A$  and  $L$  are the shape factor controlling the mass distribution described by Pfeiffer et al. (2005), where  $\lambda=2$  results in more mass distributed in the lower portion of the plume. The *FPlume* approach (Folch et al., 2016) was solved for mass flow rate (MFR, Degruyter and Bonadonna (2012)). Two total grain-size distributions (TGSD) were tested including a field-based Gaussian (*Mod*  $\Phi$  and  $\sigma\text{-}\Phi$  of 1.7 and 3.1, respectively; Bonadonna et al., 2015) and a model-based Bi-Weibull (modes at -3.13 and 4.69  $\Phi$  with respective shape factors of 0.73 and 1.1  $\Phi$  and a mixing factor of 0.64; Costa et al., 2016, Folch et al., 2021) distributions.



LC	Impact	Optimisation					Model metrics							
		Max depth	Learning rate	Alpha	Lambda	Min Child Weight	Mean MAE	Std MAE	Mean R2	Std R2	Mean MAE	Std MAE	Mean R2	Std R2
All	minV	11	0.037	0.065	5.833	17.548	0.046	0.001	0.936	0.013	0.061	0.003	0.906	0.029
	minT	12	0.040	0.133	0.396	12.971	194.874	5.811	0.700	0.014	251.854	8.498	0.577	0.023
Crops	minV	10	0.046	0.094	8.576	10.157	0.062	0.006	0.847	0.042	0.100	0.010	0.707	0.053
	minT	12	0.045	0.216	0.157	15.980	202.460	16.591	0.651	0.039	304.758	28.692	0.470	0.085
Herbaceous	minV	12	0.050	0.116	1.274	21.702	0.040	0.004	0.955	0.043	0.053	0.008	0.907	0.069
	minT	12	0.043	0.525	0.0005	10.032	171.563	11.755	0.716	0.034	216.754	17.310	0.586	0.061
Shrubs	minV	11	0.046	0.094	0.0004	39.336	0.042	0.005	0.671	0.162	0.046	0.008	0.566	0.206
	minT	12	0.050	0.048	0.008	40.583	189.501	14.768	0.593	0.055	207.409	19.116	0.515	0.073
Sparse	minV	10	0.050	0.073	1.949	67.089	0.039	0.003	0.733	0.239	0.049	0.009	0.428	0.259
	minT	10	0.047	0.284	0.001	22.610	225.702	11.477	0.459	0.060	245.865	19.722	0.386	0.084
Forest	minV	10	0.049	0.123	2.117	10.999	0.075	0.005	0.894	0.030	0.096	0.008	0.872	0.045
	minT	11	0.049	0.012	0.023	16.667	253.507	15.858	0.669	0.034	332.919	18.864	0.543	0.041

**Table 4** : Summary of the trained models. The *Optimisation* columns group reports the hyperparameter values obtained with the optimisation process. The *Model metrics* columns group reports the mean absolute error (MAE) and the  $r^2$  coefficients on both training and test datasets. The mean and the standard deviation (Std) were obtained by 5-fold cross validation with three repeats.



Importance:	minV												minT														
	SHAP						Permutation importance						SHAP						Permutation importance								
	A	Cro	Her	Shru	Spar	Fore	A	Cro	Her	Shru	Spar	Fore	A	Cro	Her	Shru	Spar	Fore	A	Cro	Her	Shru	Spar	Fore			
minV_EVI_CDI	11	19	24	24	32	18	11	19	24	24	29	32	20	11	19	24	24	29	32	20	11	19	24	24	29	32	20
EVI	2	2	2	3	3	2	2	2	2	3	6	2	1	1	1	1	1	1	1	1	1	1	1	1	1		
elevation	3	6	6	5	1	3	3	8	8	9	1	4	4	4	2	5	7	4	4	4	2	5	7	4			
EVI_stdDev	5	5	9	8	12	7	5	6	6	10	13	9	3	8	5	3	2	3	3	6	4	3	3	3			
lapilli	1	11	1	1	2	1	1	5	1	1	10	1	2	2	6	4	5	7	2	2	3	4	6	6			
fine_ash	6	4	14	12	9	4	8	4	9	2	5	6	6	18	9	19	9	2	6	13	8	20	11	2			
coarse_ash	4	10	4	7	4	6	6	11	5	5	9	7	7	5	4	11	12	5	7	7	5	5	10	13			
slope	8	8	8	13	16	9	9	7	7	11	14	11	9	13	14	8	4	12	1	17	15	7	4	12			
total_precipitation_SRI_3	2	9	10	9	8	21	2	9	10	17	20	23	8	3	11	17	8	8	8	3	9	13	10	8			
northness	1	7	14	19	20	13	1	3	12	15	19	12	1	6	6	8	10	16	1	5	7	7	15	9			
total_precipitation_SRI_2	1	3	14	19	20	13	1	3	12	15	19	12	1	3	14	17	14	6	1	2	19	20	2	5			
total_precipitation_SRI_1	2	3	29	18	14	17	2	3	30	20	7	21	3	14	17	2	11	25	1	2	19	20	2	22			
total_precipitation_SRI	5	7	18	10	13	30	2	2	10	22	16	26	5	23	13	9	17	10	5	26	16	8	17	11			
temperature_2m_S	1	17	5	4	11	16	1	18	4	8	21	18	1	5	21	7	15	27	1	1	20	10	18	21			
eastness	1	13	21	23	19	14	6	13	18	21	12	13	1	7	15	13	16	11	1	4	11	14	12	20			
total_precipitation_SRI_1	9	13	21	23	19	14	6	13	18	21	12	13	1	7	15	13	16	11	1	4	11	14	12	20			
total_precipitation_SRI_1	1	22	17	30	24	5	1	19	19	30	22	10	1	10	12	24	15	21	1	3	15	18	22	12			
total_precipitation_SRI_4	3	26	13	6	5	23	2	5	27	16	16	25	2	2	20	19	18	22	1	1	7	14	13	19			
wind_10	3	20	16	19	26	10	4	15	17	23	26	8	2	2	7	29	21	26	1	9	9	25	23	14			
temperature_2m	1	23	25	31	23	8	4	24	14	31	18	3	2	2	22	18	10	18	2	2	23	17	11	19			
temperature_2m_S	1	18	11	16	28	25	7	20	13	14	29	27	8	8	22	18	10	18	2	2	23	17	11	19			
temperature_2m_S	8	18	11	16	28	25	7	20	13	14	29	27	8	8	22	18	10	18	2	2	23	17	11	19			
aspect	2	16	26	29	31	15	2	17	25	25	28	17	7	11	27	14	23	17	3	3	10	24	17	24			
total_precipitation_3	4	30	3	22	21	33	3	30	3	28	11	32	1	9	12	23	20	22	0	0	12	23	21	22			
soil	3	30	3	22	21	33	3	30	3	28	11	32	1	1	28	21	19	15	1	6	27	28	6	18			
temperature_2m_S	9	12	15	26	17	28	1	14	20	32	24	30	2	2	19	16	23	21	2	2	21	12	25	23			
climate	2	15	22	11	10	24	2	16	28	6	19	29	1	2	24	25	29	25	2	6	22	27	29	28			
handform	5	1	7	14	22	12	2	9	11	15	27	14	3	4	29	34	34	20	3	3	29	34	31	34			
handform	2	19	24	24	32	18	4	22	24	29	32	20	2	2	17	22	28	26	2	7	16	22	27	26			



temperature_2m_s	2	21	20	27	18	27	2	21	27	27	17	28	2	25	24	25	29	19	2	25	26	24	29	20
total_precipitation	1	29	30	<b>2</b>	33	26	8	28	21	4	33	19	0	16	32	12	33	36	3	18	33	16	31	35
temperature_2m_s	2	28	27	17	15	20	7	29	29	8	22	22	3	26	28	30	28	24	3	24	30	26	30	24
total_precipitation	2	24	31	15	34	22	6	23	31	13	34	15	2	30	31	26	<b>3</b>	28	4	28	31	28	<b>2</b>	32
temperature_2m_3	3	25	23	33	20	31	3	26	23	26	15	31	4	33	20	31	31	14	2	33	19	32	32	13
total_precipitation	3	34	33	28	29	35	3	34	33	33	31	35	3	34	<b>3</b>	<b>6</b>	<b>6</b>	35	3	34	<b>6</b>	<b>9</b>	<b>8</b>	34
temperature_2m_1	2	27	32	34	27	11	1	25	32	34	25	<b>5</b>	1	27	30	32	30	33	2	30	29	34	27	33
handcover	8	35	24	35	35	19	1	35	24	35	35	16	4	36	36,5	36	36	30	1	36	36	36	36	30
total_precipitation	3	31	28	21	30	29	3	32	26	24	30	24	3	31	26	33	27	32	3	32	21	33	25	28
temperature_2m_2	3	32	34	25	<b>7</b>	32	3	31	35	18	<b>3</b>	33	0	32	33	35	35	34	2	31	32	35	35	36
temperature_2m_4	3	33	35	32	<b>6</b>	34	3	33	34	22	<b>2</b>	34	3	35	35	27	32	29	3	35	36	30	33	31

**Table 5** : Ranking of feature importance computed using mean absolute SHAP values and permutation importance for all landcover class and impact metrics. A darker cell colour indicates a stronger importance. For each column, the 3 most important features are in bold and the 10 most important features are in red.